INTERNATIONAL SCIENTIFIC JOURNAL

MATHEMATICAL MODELING

YEAR Y, ISSUE 3/2021
ISSN (PRINT) 2535-0986
ISSN (WEB) 2603-2929

Published by
SCIENTIFIC-TECHNICAL UNION of MECHANICAL ENGINEERING - INDUSTRY 4.0
Sofia, BULGARIA

INTERNATIONAL EDITORIAL BOARD

EDITOR I CHIEF	
Prof. ANDREY FIRSOV Peter the Great St.Petersburg Polytechnic University	RU

Members:		
Abilmazhin Adamov, Prof.	L.N.Gumilyov Eurasian National University	KZ
Alexander Guts, Prof.	Omsk State University	RU
Alexei Zhabko, Prof.	Saint Petersburg State University	RU
Andrey Markov, Prof.	Baltic State Technical University	RU
Andrii Matviichuk, Prof.	Kyiv National Economics University	UA
Andrzej Nowakowski, Prof.	University of Lodz	PL
Anton Makarov, Dr.	Saint Petersburg State University	RU
Armands Gricans, Assoc. Prof.	Daugavpils University	LV
Artūras Dubickas, Prof.	Vilnius University	LT
Avinir Makarov, Prof.	Saint Petersburg State University of Industrial Technologies and Design	RU
Christo Boyadjiev, Prof.	Institute of Chemical Engineering, BAS	BG
Daniela Marinova, Dssoc. Prof.	Technical University of Sofia	BG
Dimitrios Poulakis, Prof.	Aristotle University of Thessaloniki	GR
Evgeniy Smirnov, Assoc. Prof.	Volgograd State Technical University	RU
Galia Angelova, Prof. DSc,	Bulgarian Academy of Science	BG
Giovanni Borgioli, Assoc. Prof.	University of Florence	IT
Haskiz Coskun, Prof.	Karadeniz Technical University of Trabzon	TR
Idilia Bachkova, Prof.	University of Chemical Technology and Metallurgy	BG
Igor Anufriev, Assoc. Prof.	Peter the Great St.Petersburg Polytechnic University	RU
Irena Stojkovska, Prof.	Ss. Cyril and Methodius University in Skopje	MK
Ivana Štajner-Papuga, Prof.	University of Novi Sad	RS
Kanagat Aldazharov, Assoc. Prof.	Kazakh Economics University	KZ
Karl Kunisch, Prof.	University of Graz	AT
Mahomed Agamirza ogly Dunyamalyev, Prof.	Azerbaijan Technical University	AZ
Marius Giuclea, Prof.	The Bucharest University of Economics Studies	RO
Mihail Okrepilov, Prof.	D.I. Mendeleyev Institute for Metrology (VNIIM)	RU
Milena Racheva, Assoc. Prof.	Technical University of Gabrovo	BG
Mohamed Kara, Dr.	Ferhat Abbas Sétif 1 University	DZ
Mohamed Taher El-mayah, Prof	MTI University	EG
Neli Dimitrova, Prof.	Institute of Mathematics and Informatics, BAS	BG
Nina Bijedic, Prof.	Dzemal Bijedic University of Mostar	BA
Oleg Obradović, Prof.	University of Montenegro	ME
Olga Pritomanova, Assoc. Prof.	Oles Honchar Dnipropetrovsk National University	UA
Özkan Öcalan, Prof.	Akdeniz University of Antalya	TR
Paşc Găvruţă, Prof.	Politehnic University of Timisoara	RO
Pavel Satrapa, Assoc. Prof.	Technical University of Liberec	CZ
Pavel Tvrdík, Prof.	Czech Technical University in Prague	CZ
Pavlina Yordanova, Assoc. Prof.	Shumen University	BG
Petr Trusov, Prof.	Perm State Technical University	RU
Rannveig Björnsdóttir, Prof.	University of Akureyri	IS
Roumen Anguelov, Prof.	University of Pretoria	ZA
Sándor Szabó, Dr. Prof.	University of Pécs	HU
Sashko Martinovski, Assoc. Prof.	St. Kliment Ohridski University of Bitola	MK
Sergey Bosnyakov, Prof.	Moscow Institute of Physics and Technology	RU
Sergey Kshevetskii, Prof.	Immanuel Kant Baltic Federal University	RU
Snejana Hristova, Prof.	University of Plovdiv	BG
Svetlana Lebed, Assoc. Prof.	Brest State Technical University	BY
Tomasz Szarek, Prof.	University of Gdansk	PL
Valeriy Serov, Prof.	University of Oulu	FI
Vasily Maximov, Prof.	Saint Petersburg State University of Industrial Technologies and Design	RU
Ventsi Rumchev, Prof.	Curtin University, Perth	AU
Veronika Stoffová, Prof.	University of Trnava	SK
Veselka Pavlova, Prof.	University of National and World Economy	BG
Viorica Sudacevschi, Assoc. Prof.	Technical University of Moldova	MD
Vladimir Janković, Prof.	University of Belgrade	RS
Vladislav Holodnov, Prof.	Saint Petersburg State Institute of Technology	RU
Vyacheslav Demidov, Prof.	Saint Petersburg State University of Industrial Technologies and Design	RU
Yordan Yordanov, Assoc. Prof.	University of Sofia	BG
Yuriy Kuznetsov, Prof.	Nizhny Novgorod State University	RU
Zdenka Kolar - Begović, Prof.	University of Osijek	HR

INTERNATIONAL SCIENTIFIC JOURNAL

MATHEMATICAL MODELING

PUBLISHER:

SCIENTIFIC TECHNICAL UNION OF MECHANICAL ENGINEERING "INDUSTRY 4.0"

108, Rakovski Str., 1000 Sofia, Bulgaria
tel. (+359 2) 987 72 90,
tel./fax (+359 2) 986 22 40**,**
office@stumejournals.com
www.stumejournals.com

ISSN (PRINT) 2535-0986
ISSN (WEB) 2603-2929
YEAR V, ISSUE 3 / 2021

EDITOR IN CHIEF:

Prof. D.Sc. ANDREY FIRSOV
Peter the Great St.Petersburg Polytechnic University, Russia

CONTENTS

THEORETICAL FOUNDATIONS AND SPECIFICITY OF MATHEMATICAL MODELLING

Study of the model for estimating the degree of influence of distortion on image quality with the application of an entropic measure
David Asatryan, Mariam Haroutunian, Grigor Sazhumyan 83

Influence of data points density on geometrical accuracy of interpolation surface
Marta Hlavová, Ivana Linkeová 86

MATHEMATICAL MODELLING OF TECHNOLOGICAL PROCESSES AND SYSTEMS

Temperature field in a layered plate with local heating
Vasyl Havrysh, Liubov Koliasa, Svitlana Vozna 90

Modeling transient signals in power lines
Rustem Khuziashev, Igor Kuzmin, Ildar Minaev 95

Validation MAGMA model of welding process
Deyan Gradinarov, Georgi Georgiev 99

Investigation of bending strength and modulus of elasticity of a new type of black locust plywood for construction
Asen Hristov, Valerii Naidenov, Lilyana Koleva 101

Modelling uncertainty in multisensory systems at conflict measurements with dempster-shafer combinatorial rule
Varbanov Vladimir 104

MATHEMATICAL MODELLING OF SOCIO-ECONOMIC PROCESSES AND SYSTEMS

Adiabatical thermodynamic manner of the description of the carbon dioxide pollutant excess of Earth's atmosphere
Mihai Petrov 106

MATHEMATICAL MODELLING OF MEDICAL-BIOLOGICAL PROCESSES AND SYSTEMS

Smoluchowski's coagulation equation with injections: applications to clustering of nano-particles
Dmitri Alexandrov, Ilya Starodumov, Sergei Fedotov, Alexander Ivanov, Irina Alexandrova, Eugenya Makoveeva 112

Study of the model for estimating the degree of influence of distortion on image quality with the application of an entropic measure

David Asatryan[1], Mariam Haroutunian[1,*], Grigor Sazhumyan[1]
Institute for Informatics and Automation Problems of NAS, Yerevan, Armenia[1]
armar@sci.am [*]

Abstract: *The article deals with the problem of comparative analysis of the experimental results of using standard-free quality assessment measures depending on the type of distortion applied to the image. The previously developed measure based on the Weibullian model of the gradient magnitude and the entropy measures applied both to the original image and to the gradient characteristics of the image are considered as No-Reference quality measures. Weibull distribution parameters are estimating using a set of image gradient magnitudes using the Sobel operator. A series of experiments was carried out on texture images from the well-known Brodatz texture database and the TID2013 database, which contains images distorted by various types. It was observed that texture images are in good agreement with the Weibullian model, which makes it possible to effectively apply the above-mentioned No-Reference measures and carry out a comparative analysis. The use of the TID2013 database with 3000 images, distorted by 24 types, each at five levels, makes it possible to evaluate additionally the effectiveness of the entropy approach to assessing image quality, comparing them with visual assessments also given in the database. Then it was illustrated that applying the entropy approach directly to the original image gives a worse result than applying image gradients to the magnitude. At the same time, a higher sensitivity to structural changes from the level and type of applied distortions is observed. The problem of the expediency of calculating the entropy using estimates of the parameters of the Weibull distribution instead of the histogram of the array of gradient magnitudes is investigated separately. The paper contains numerical and graphical materials illustrating the obtained results.*

Keywords*: IMAGE QUALITY, DISTORTION, NO-REFERENCE MEASURE, WEIBULL DISTRIBUTION, GRADIENT MAGNITUDE, ENTROPY, STRUCTURAL PROPERTIES*

1. Introduction

The problem of quality assessment is one of the central problems in the field of digital image processing. As it is known, almost any action on image processing inevitably faces this problem, since processing involves certain transformations of the image description data, and the final result of performing actions is evaluated visually or by formal methods [1].

The use of formal methods becomes especially important in the automatic processing of large-volume images, when human participation in assessing their quality is difficult, and often impossible. Therefore, in recent years, methods for assessing image quality by formal methods and comparing the result with subjective assessments of the human visual system (HVS), previously established by a group of experts for a sufficiently large number of images, have become popular (see, for example, [2, 3]). At the same time, such information is used not only for individual assessment of an image quality, but also for assessing the effectiveness of the method used itself.

In the scientific literature, a large number of methods and means for assessing image quality have been proposed using various approaches and methods for their implementation. In [4], a detailed review of the state of the Image quality assessment problem and the formulation of unresolved problems by that time was carried out. It can be stated that many of the problems presented in this work have not yet been solved, although intensive research in this direction continues. However, a review of these methods within the framework of a limited article does not seem appropriate, so we will focus only on the methods that are directly related to the topics discussed.

First of all, we note that all quality assessment methods are grouped around two main approaches. The first approach involves comparing two images, one of which is considered a reference (original), and the second is a tested image obtained after applying certain transformations, which resulted in its distortion. This method is called the Full-Reference (FR) method and has been used for a long time, based, in particular, on methods from the field of signal processing. For example, the standard deviation of two pixel intensity matrices and its various modifications are used. A critical analysis of these methods when assessing the quality of images and a proposal for a new approach is given in [5, 6], stimulating the rapid growth of improvements and applications of this approach.

The second approach is used when there is no reference image and it is necessary to understand the structure of the tested image and use only the information available in it. This method is called No-Reference (NR) and is also widely used. Let us indicate only a few that are most closely related to the issues under discussion [7-12].

In this work, we restrict ourselves to standard less methods based on the entropy measure, comparing it in terms of efficiency with other measures, based on the above-mentioned estimates of the quality of the HVS for certain classes of images.

Note that the entropy measure is increasingly used in applied problems, in which the uncertainty estimated by the entropy of an image and / or its certain characteristics can be interpreted as an assessment of its quality (for example, let us refer to [13]).

The aim of this work is to experimentally study the effectiveness of the entropy measure for assessing the effect of the type of distortion on image quality by comparing with other measures using subjective quality assessments.

2. Research Technique

Weibull distribution based Model. Following [14], we will accept for the gradient magnitude of the image a model based on the Weibull distribution, the density of which is given by the formula

$$f(x;\lambda,\eta)=\frac{\eta}{\lambda}\left(\frac{x}{\lambda}\right)^{\eta-1}\exp\left[-\left(\frac{x}{\lambda}\right)^{\eta}\right],\ x\geq 0, \tag{1}$$

where $\eta > 0$ is the shape parameter, $\lambda > 0$ is the scale parameter. The gradient magnitudes are estimated using the Sobel operator, and the parameters of distribution (1) are estimated from the totality of all magnitudes. Details of the procedure and the corresponding experimental results can be found in [14-16].

Following [11], we will take the value of the parameter η as a measure characterizing the image quality (the lower the value of the measure, the higher the quality).

Entropy measure for evaluating image quality. We will use the classical definition of entropy given by the formula

$$E_H=-\sum_{i=0}^{n}p_i\ln p_i \tag{2}$$

for evaluating the quality of both the tested image and visualized by using the set of the gradient magnitudes.

Let us note one kind of application of the entropy measure. If the parameters of the Weibull distribution are known, then we can use the well-known approximate formula for the entropy

$$E_W\approx -0.57722\left(1-\frac{1}{\eta}\right)+Ln\left(\frac{\lambda}{\eta}\right)+1. \tag{3}$$

The paper analyzes the two formulas given in terms of accuracy and appropriateness of their application.

Used image databases. Several databases are available in the literature, some of which contain expert assessments of image quality. However, in the current work, only the well-known texture image databases Brodatz and the base TID2013 are used. The Brodatz texture database includes 112 images. The TID2013

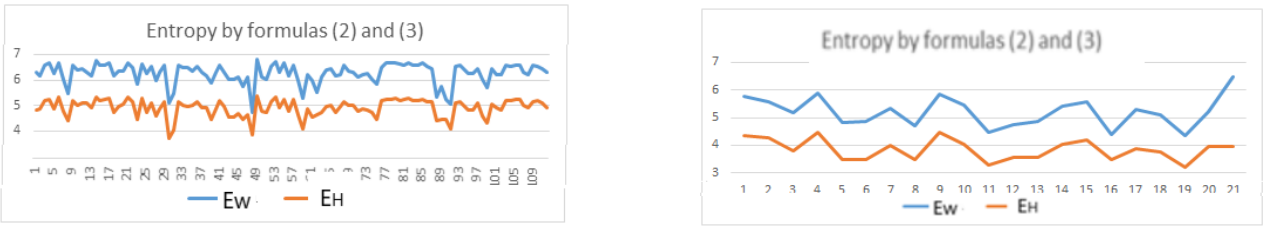
database [2] contains 3000 images obtained from 25 originals, distorted by 24 different types with five levels each. Further, an extensive experiment was carried out on the visual assessment of quality according to a point system by a large number of people in different countries. As a result of processing these data, each of 3000 images was assigned a numerical assessment of the quality of the HVS and fixed the Mean Opinion Score - MOS).

The use of the TID2013 database makes it possible to evaluate the quality of any procedure used in the problem of image quality assessment by both the FR method and the NR method, and the decision on the quality of the procedure is made according to the degree of correlation of the procedure estimates with the MOS values.

3. *Experimental Results*

Experiment 1. Comparative analysis of formulas (2) and (3). The entropy of the magnitudes of the gradients of 112 images of the Brodatz database and 25 original images of the TID2013 database was calculated using formulas (2) and (3). The results are shown in Fig. 1 in the form of graphs, in which the data for the entropy E_W are shown in blue (upper curve), and for the entropy E_H - in red (lower curve). As expected, the E_W entropy values calculated using the Weibull parameter estimates slightly exceed the E_H values calculated from the histogram. The reason lies in the fact that the Weibull distribution is a model that only approximately describes the behavior of the gradient magnitude, therefore, additional uncertainty appears, due to which the entropy increases. The graphs also show that the nature of the change in the values of entropy is practically the same for both formulas. It can also be seen that the graph in Fig. 1a, the divergence of the curves is less than in the graph in Fig. 1b, which is explained by the better agreement with the Weibull distribution in the case of texture images.

These facts allow us to apply both formulas in problems of image quality estimation.



(a) (b)

Figure 1. Curves of changes in the entropy of images, calculated by formulas (2) and (3). (a) - for images from the Brodatz base; (b) *- for images from the TID2013 database.*

Experiment 2. Comparison of the entropy measure with expert estimates of image quality. An extensive experiment was carried out to assess the quality of images and compare with expert estimates and analyze the results obtained.

Correlation of image characteristics. The calculations of the following images of the images of the TID2013 database were carried out: the shape parameter η of the Weibull distribution, the values of the entropies E (for the original image), E_W and E_H, calculated by formulas (2) and (3) for the gradient magnitudes. Table 1 shows a fragment of the results of calculations for image 1 type of image of five levels and the results of expert evaluations of MOS. For comparison, the shape parameters η of the Weibull distribution are also given, the study of which as a measure of quality was carried out in [11, 12]. These data can illustrate the main details of the research methodology proposed in the work.

Table 1: *Fragment of calculation results*

	Estimated values of the parameters					SCC with MOS			
Name	η	**E**	E_W	E_H	**MOS**	η	**E**	E_W	E_H
I01_01_1.bmp	1.05	4.94	5.65	4.894	5.51429				
i01_01_2.bmp	1.08	4.96	5.66	4.900	5.56757				
i01_01_3.bmp	1.13	4.99	5.69	4.915	4.94444	-0.9	-0.9	-0.9	-0.9
i01_01_4.bmp	1.21	5.05	5.74	4.946	4.37838				
i01_01_5.bmp	1.33	5.14	5.79	5.003	3.86486				
i01_02_1.bmp	1.02	4.93	5.63	4.890	6.02857				
i01_02_2.bmp	1.03	4.95	5.64	4.891	6.10811				
i01_02_3.bmp	1.05	4.99	5.65	4.894	5.38889	-0.9	-0.9	-0.9	-0.9
i01_02_4.bmp	1.08	5.04	5.66	4.901	4.71429				
i01_02_5.bmp	1.13	5.14	5.69	4.916	4.36111				
i01_03_1.bmp	1.06	4.94	5.65	4.895	4.77143				
i01_03_2.bmp	1.10	4.95	5.68	4.906	4.27027				
i01_03_3.bmp	1.16	4.99	5.71	4.929	3.70270	-1	-1	-1	-1
i01_03_4.bmp	1.26	5.05	5.76	4.964	3.19444				
i01_03_5.bmp	1.40	5.14	5.83	5.0387	2.71429				

The last four columns of Table 1 show the values of the Spearman correlation coefficient (SCC) of the considered parameters with MOS, the formula for which is given by the expression

(4) $$SCC = 1 - 6\sum_{j=1}^{5}(x_i - y_i)^2 /120,$$

where x_i and y_i are the ranks of the compared sequences.

The *analysis of the results* showed, in general, a high correlation of all the given quality measures, but it should be noted that the values given in Table 1 are not typical for all base images and types of distortions. The result of calculating the correlation of a No-Reference quality measure with subjective assessments depends both on the structural properties of the tested image and on the type and intensity of the applied distorting method. However, analyzing the results of calculations across the entire TID2013 database, we can note some patterns that characterize the effectiveness of the proposed approach.

a) The Weibull distribution shape parameter and entropy are quite reliable means for an image quality assessing, which have a close correlation with subjective MOS estimates. This allows these tools to be used stand-alone for any type of image without using MOS scores.

b) The values of the entropy E_H, calculated using the

gradient magnitudes, are usually less than the values of E, which is an additional confirmation of the effectiveness of the usage of gradient methods.

c) The values of the entropy E_W, calculated using the estimates of the Weibull distribution parameters, slightly exceed the values of E_H calculated from the histogram of the gradient magnitudes. The reason, as mentioned above, lies in the fact that the Weibull distribution only approximately describes the behavior of the gradient magnitude. However, formula (3) with known estimates of distribution parameters is preferable to histogram methods in view of the simplicity of calculations.

d) The results of images processing obtained with different types of distortions may differ significantly. For the types of distortions that distort the structure of the image, correlations are weaker because gradient methods inherently respond to the structural properties of the image. As an example, let us indicate the type of distortion 18 Change of color saturation [2]. There are numerical results of analysis for other types of distortions, showing the degree of influence on image quality, taking into account their ability to destroy the image structure.

4. Conclusion

Thus, the study performed has shown that the information-theoretical approach to the problem of image quality assessment is very useful, and entropy can be used as a standard-free measure on its own without involving a visual method, as well as in combination with other methods.

5. References

1. V. A. Soyfer (Ed.), *Methods of computer image processing*; (in russian), Physmatlit, (2003).
2. N. Ponomarenko, L. Jin, O. Ieremeiev, V. Lukin, K., Egiazarian, J. Astola, B. Vozel, K. Chehdi, M. Carli, F. Battisti, et al., Signal Proc.: Image Communication, **30**, 57–77, (2015).
3. H. Sheikh, Z. Wang, L. Cormack, A. Bovik, http://live.ece.utexas.edu/research/quality .
4. D. M. Chandler, ISRN Signal Process, 1–53, (2013).
5. Z. Wang, A. C. Bovik, IEEE Signal Proc. Letters, **9(3)**, 81–84, (2002).
6. Z. Wang, A.C. Bovik, H.R. Sheikh, E.P. Simoncelli, IEEE Trans. Image Process., **13(4)**, pp. 600– 612, (2004).
7. S. S. Hemami, A. R. Reibman, Signal Process. Image Commun, **25(7)**, 469–481, (2010).
8. V. Kamble, K. M. Bhurchandi, Optik – Int. J. Light and Electron Optics, **126 (11-12)**,1090-1097, (2015).
9. E. Cohen, Y. Yitzhaky, Signal, Image and Video Proc., **4(3)**, 289–302, (2010).
10. V. V. Starovoitov, F. V. Starovoitov, Systems Analysis and Applied Informatics **1**, 24-32 (in russian), (2017).
11. D. Asatryan, Computer Optics, **41(6)**, 957-962, (2017).
12. D. Asatryan, in: *Int. Conf. CSIT*, Yerevan, Armenia, 201–203, (2019).
13. F. Escolano, P. Suau, B. Bonev, *Information Theory in Computer Vision and Pattern Recognition*. Springer-Verlag, (2009).
14. D. Asatryan, K. Egiazarian, in: *Int. Workshop Local and Non-Local Approximation in Image Processing*, Finland, Helsinki, 70-73, (2009).
15. D. G. Asatryan, Computer Optics; **43(2)**, 245-250, (2019).
16. D. G. Asatryan, M. E. Haroutunian, Y. I. Golub, V. V. Starovoitov, System analysis and applied information science, **3**, 22-27, (2020).

Acknowledgment

This work was supported by the Russian Foundation for Basic Research and RA Science Committee in the frames of the joint research project RFBR 20-51-05008 Arm a and SCS 20RF-144 accordingly.

Influence of data points density on geometrical accuracy of interpolation surface

Marta Hlavová, Ivana Linkeová
Faculty of Mechanical Engineering, Czech Technical University in Prague, Czech Republic
marta.hlavova@fs.cvut.cz

Abstract: *Interpolation is one of widely used methods reconstructing the shape of a freeform surface from data points obtained by measurement. The geometrical accuracy of the resulting reconstructed surface is expressed as a range of normal deviations of the surface from the original shape and depends mainly on the density of the input data points. In the paper, a method to determine the geometrical accuracy of the interpolation surface fitted through a set of definition points arranged in a structured quadrilateral mesh with a given density is described. Practical application of this method is demonstrated on the processing of experimental data mathematically generated from a known CAD model of suitably chosen freeform surface.*

Keywords*: CAD, GEOMETRICAL ACCURACY, INTERPOLATION B-SPLINE SURFACE, FREEFORM SURFACE*

1. Introduction

For a shape reconstruction of a freeform surface with no CAD (Computer Aided Design) model available, a digitization, i.e. transformation of a point data obtained by measurement of the original shape into a computer-readable representation is a key operation. There are two different approaches to digitize an unknown surface – triangulation (linear reconstruction) [1, 2] and freeform surface fitting [3, 4]. Triangulation is widely used when processing unstructured input data in a form of point clouds, usually generated by optical scanning [5] of real objects. In case that the input data are ordered into a structured quadrilateral mesh, the freeform surface fitting approach is more suitable. Such input data can be generated by tactile point to point measurement on CMM (Coordinate Measuring Machine), for example.

When using freeform surface fitting approach, it is always necessary to find a compromise between smoothness and continuity of the fitted surface and its shape deviation from the original object [3, 6]. This shape deviation strongly depends on the density of the input points. In this paper, we focus on the determination of geometrical accuracy of CAD model of a freeform surface assuming the CAD model in form of interpolation B-spline surface [7] passing through a set of structured definition points. In the following, this model is referred to as the interpolation CAD model. The geometrical accuracy of CAD model corresponds to the application in which the model is used. For example, if the interpolation CAD model is intended as a representation of reference CAD model in precision tactile CAD-based freeform metrology, the shape conformity of the interpolation CAD model with the measured surface has to be comparable to or less than measurement uncertainty of CMM [8, 9]. Measurement uncertainty is related to the MPE (Maximum Permissible Error) defined as the extreme value of an error permitted by specifications between the indication of a measuring instrument and the corresponding true value [10]. MPE is proportional to the measured length and its constant value ranges from tenths of micrometers for the most precise tactile CMM to tens of micrometers for portable CMM and optical scanners.

This paper is organized as follows. Section 2 briefly reminds basic knowledges about commonly used interpolation methods, Section 3 describes the process to derive geometrical accuracy of interpolation B-spline surface for given density of definition points. In section 4, the proposed method is demonstrated and verified on experimental data processing. Section 5 summarizes the achieved results and gives directions for the future research work.

2. Interpolation B-spline Surfaces

To get a freeform surface CAD model passing through $(m+1)\times(n+1)$ points arranged in a structured bidirectional mesh, using the interpolation B-spline surface is the simplest solution. Given points are considered as definition points $\mathbf{Q}_{i,j}$ $(i=0,\dots,m,$ $j=0,\dots,n)$ of this interpolation B-spline surface and the degrees of B-spline basis functions [7] are set equal to 3, which is sufficient to maintain smoothness and C^2 continuity of the resulting CAD model. Due to the different approaches for creating such interpolation surface, there are two main types of results – global and local bicubic interpolation B-spline surfaces [7]. However, both bicubic interpolation B-spline surfaces can be also defined as bicubic approximation B-spline surfaces by set of control points that are different from the original definition points. In case of global interpolation, the number of control points is $(m+1)\times(n+1)$ and this surface is composed from $(m-2)\times(n-2)$ individual patches that are connected in order to fulfill C^2 continuity condition. Considering the local interpolation, the number of control points is increased to $(m+3)\times(n+3)$ and such interpolation bicubic surface is composed from $m\times n$ individual patches connected with C^2 continuity. Both cases of interpolation B-spline surfaces with its control point meshes and displayed segmentations are depicted in Fig. 1.

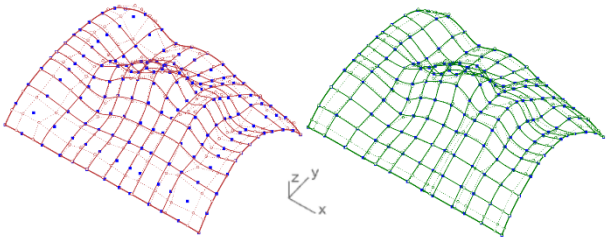


Fig. 1 *Global interpolation B-spline surface (on the left, red), local interpolation B-spline surface (on the right, green), interpolated points (blue).*

One of the features of local interpolation (see Fig. 1, on the right) is that the corner points of any individual patch are the original definition points. This property can be used to derive a dependence of geometrical accuracy of surface on density of definition points as is described in the following section.

3. Geometrical Accuracy of Open Bicubic Uniform B-spline Surface

Suppose single individual patch of local interpolation bicubic B-spline surface with 4 original definition points at its corners. This patch can be considered Bézier bicubic patch [7] determined by 4×4 control points $\mathbf{V}_{i,j}, (i=0,\dots,3, j=0,\dots,3)$ arranged into quadrilateral mesh to set 4 original definition points as corners $\mathbf{V}_{0,0}, \mathbf{V}_{3,0}, \mathbf{V}_{0,3}, \mathbf{V}_{3,3}$ of this mesh to interpolate them. Thus, every individual patch can be considered an open approximation bicubic uniform B-spline surface with special B-spline third degree basis functions

$$C_0(t)=\frac{1}{6}(1-t)^3$$
$$C_1(t)=\frac{1}{6}(3t^3-6t^2+4)$$
$$C_2(t)=\frac{1}{6}(-3t^3+3t^2+3t+1)$$

$$C_3(t) = \frac{1}{6}t^3.$$

This single-segment open bicubic uniform B-spline surface $\boldsymbol{T}(u,v)$ is defined by 4×4 control points $\mathbf{P}_{i,j}$, $(i = 0,\dots,3,\ j = 0,\dots,3)$ and

$$(1) \qquad \boldsymbol{T}(u,v) = \sum_{i=0}^{3}\sum_{j=0}^{3} C_i(u)C_j(v)\mathbf{P}_{i,j}, (u,v) \in [0,1]^2.$$

Example of such a surface is shown in Fig. 2. Due to the relationship between Bézier and B-spline approximation surfaces, the control points $\mathbf{V}_{0,0}, \mathbf{V}_{3,0}, \mathbf{V}_{0,3}, \mathbf{V}_{3,3}$ of the Bézier bicubic patch are corners of this B-spline surface $\boldsymbol{T}(u,v)$, where $\mathbf{V}_{0,0} = \boldsymbol{T}(0,0)$, $\mathbf{V}_{3,0} = \boldsymbol{T}(1,0)$, $\mathbf{V}_{0,3} = \boldsymbol{T}(0,1)$ and $\mathbf{V}_{3,3} = \boldsymbol{T}(1,1)$.

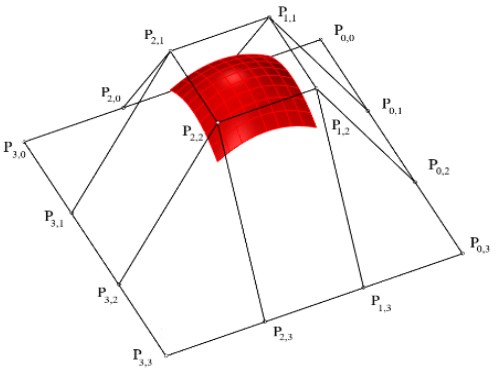


Fig. 2 *Single-segment open bicubic uniform B-spline surface (red) and its control point mesh (black).*

Geometrical accuracy of any CAD model of a surface is given by the range of normal deviations between the CAD model and the original surface and depends on the curvature of the original surface. The more curved the processed surface, the closer the data points must be for the shape reconstruction to be successful. Consequently, the worst conditions are in a neighbourhood of a point with minimum radius r of the curvature. Thus, the main idea is to estimate the geometrical accuracy of the interpolation CAD model using maximum normal deviation between a sphere κ_r with a radius r (minimum radius of curvature) and such a surface $\boldsymbol{T}(u,v)$ given by (1), the corners of which lie on the sphere κ_r. For simplicity, suppose the corners are vertices of a square, due to the same distance d of each two neighbouring corners. The distance d represents the maximum Euclidean distance of interpolation CAD model definition points and determines the density of input data points. As result, the estimation of geometrical accuracy g of the interpolation surface in dependence on the minimum radius of the curvature r of the original surface and the maximum Euclidean distance d of the two neighbouring interpolated points is expected.

The unknown control points $\mathbf{R}_{i,j}$ of the surface $\boldsymbol{T}(u,v)$ are located on the sphere κ_ϱ with the same center as the sphere κ_r and an unknown radius ϱ, see Fig. 3.

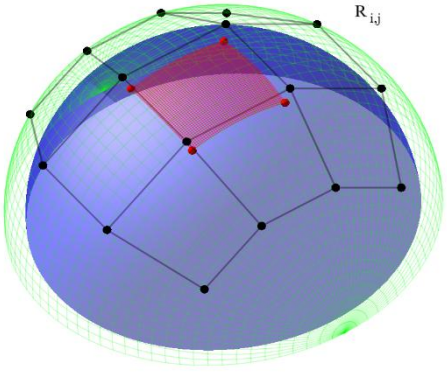


Fig. 3 *Surface $\boldsymbol{T}(u,v)$ (red) with corners on sphere κ_r (blue) and control points $\mathbf{R}_{i,j}$ (black) on sphere κ_ϱ (green).*

Without loss of generality, consider centers of both spheres κ_r and κ_ϱ at origin $\mathbf{O} = (0,0,0)$ of the coordinate system. Using transformation into spherical coordinates

$$x = \varrho\cos\varphi\cos\vartheta,$$
$$y = \varrho\sin\varphi\cos\vartheta,$$
$$z = \varrho\sin\vartheta,$$

where $\varphi \in [0,2\pi], \vartheta \in [-\pi/2, \pi/2]$, all the control points $\mathbf{R}_{i,j}$ can be represented by unique triplets $(\varrho, \varphi_{i,j}, \vartheta_{i,j})$, where angles $\varphi_{i,j}$ and $\vartheta_{i,j}$ are arranged into matrices

$$\Phi = \begin{pmatrix} -3\alpha & -\alpha & \alpha & 3\alpha \\ -3\alpha & -\alpha & \alpha & 3\alpha \\ -3\alpha & -\alpha & \alpha & 3\alpha \\ -3\alpha & -\alpha & \alpha & 3\alpha \end{pmatrix}$$

and

$$\Theta = \begin{pmatrix} 3\beta & 3\beta & 3\beta & 3\beta \\ \beta & \beta & \beta & \beta \\ -\beta & -\beta & -\beta & -\beta \\ -3\beta & -3\beta & -3\beta & -3\beta \end{pmatrix}$$

to ensure regular placement of $\mathbf{R}_{i,j}$ on the sphere κ_ϱ. Angles α, β are unknown constants.

After substituting the control points $\mathbf{R}_{i,j}$ in (1), the radius r is equal to the magnitude of a radius vector $(x_\mathbf{0}, y_\mathbf{0}, z_\mathbf{0})$ of corner $\boldsymbol{T}(0,0)$,

$$(2) \qquad r = \sqrt{x_\mathbf{0}^2 + y_\mathbf{0}^2 + z_\mathbf{0}^2}.$$

Next, equation (2) is solved to express the radius ϱ of the sphere κ_ϱ in dependence on the radius r

$$(3) \quad \varrho = \frac{9r}{(3-2\sin^2\beta)\sqrt{9-4\sin^2\beta\sin^4\alpha+4\sin^4\alpha+12\sin^2\beta\sin^2\alpha-12\sin^2\alpha}}.$$

Thus, let the corners of the surface $\boldsymbol{T}(u,v)$ lie at the vertices of a square with prescribed length d of its side. From this condition, the relation between angles α and β can be expressed by

$$(4) \qquad \beta = tan^{-1}\left(\frac{\sin\alpha\,(3 - 2\sin^2\alpha)}{3}\right).$$

The geometrical accuracy g of the surface $\boldsymbol{T}(u,v)$ (due to the sphere κ_r) is given by a maximum normal deviation of the surface $\boldsymbol{T}(u,v)$ from the sphere κ_r that occurs at point $\mathbf{W} = \boldsymbol{T}\left(\frac{1}{2},\frac{1}{2}\right)$, see Fig. 4.

Thus

$$(5) \qquad g = r - w,$$

where w is a magnitude of a radius vector $(x_\mathbf{W}, y_\mathbf{W}, z_\mathbf{W})$ of point $\mathbf{W}$,

$$w = \sqrt{x_\mathbf{W}^2 + y_\mathbf{W}^2 + z_\mathbf{W}^2}.$$

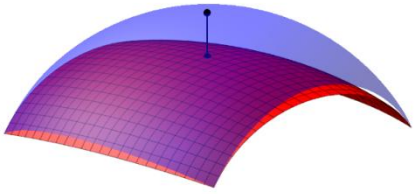


Fig. 4 *The maximum deviation of surfaces $\boldsymbol{T}(u,v)$ (red) and sphere κ_r (blue).*

Substituting (4) and (3) in (1), for prescribed distance d and the minimum radius of the curvature r, the values of angles α and β are obtained from formula for length of a square side

$$d = 2z_0$$

and these numerically obtained values are applied in (5) to compute the geometrical accuracy g.

4. Experimental Data Processing

This section demonstrates the development of an interpolation CAD models of three experimental input data sets varying in the density of these points. The data points have been generated on a test freeform surface with known CAD model in the form of clamped uniform bicubic B-spline surface, given by a mesh of 25×13 control points (see Fig. 5).

The dimensions of the test freeform surface are approximately $120\,\text{mm} \times 107\,\text{mm} \times 54\,\text{mm}$. The shape of the test freeform surface is considerably curved, see Fig. 6, where the Gaussian curvature [11] of the surface is visualized by means of a colour map obtained by surface analysis tools in Rhinoceros (3D modelling system based on NURBS representation).

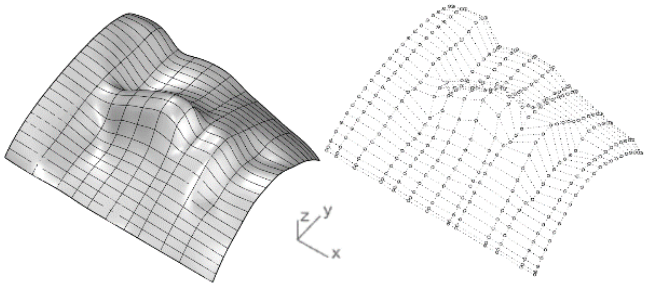


Fig. 5 *Test freeform surface*

The minimum radius of curvature of the test surface $r = 3.00327\,\text{mm}$ has been obtained in Rhinoceros diagnostics, too.

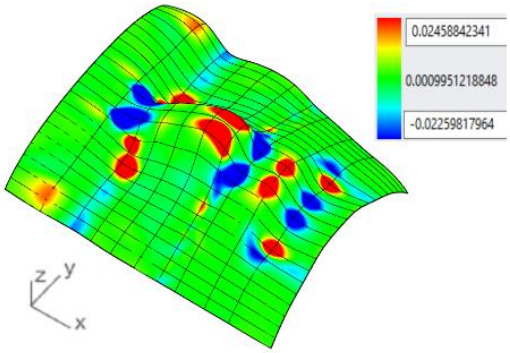


Fig. 6 *Colour map of Gaussian curvature on the test freeform surface.*

On the test freeform CAD model, the data points sets have been generated by an uniform division of two suitable selected isoparametric curves (isocurves) of the surface – specifically, both curves have been divided into 48, 96 and 192 equally long segments. For each division, data points have been created as intersections of all isocurves passing through the points of the division of the selected isocurves (see Fig. 7).

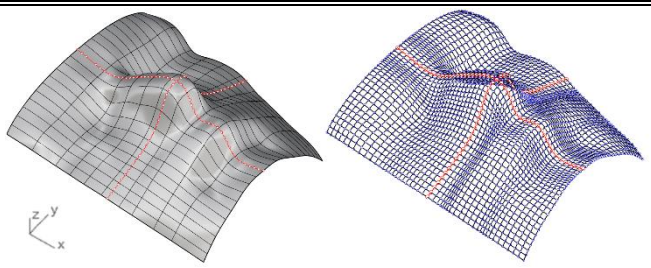


Fig. 7 *Selected isocurves and generated data points (division 48).*

All densities are shown in Fig. 8. In the following, the division of isocurves into 48, 96 or 192 segments, is reffered as division 48, 96 or 192 in the given order.

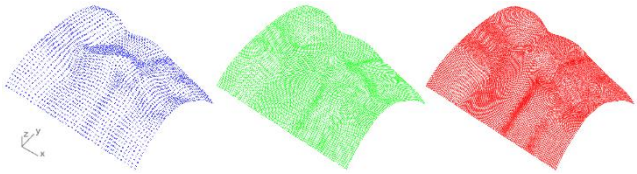


Fig. 8 *Density of sets of definition points for division 48 (blue), 96 (green) and 192 (red).*

For each density of data points given by the division 48, 96 and 192 of the selected isocurves, the maximum distance d of two neighbouring points is obtained, and then predicted geometrical accuracy g is computed by (5). Table 1 lists all these values.

Table 1: *Maximum distance d of two neighbouring definition points and computed geometrical accuracy g of local interpolation B-spline surface.*

Division [-]	Number of points [-]	Maximum distance d [mm]	Geometrical accuracy g [mm]
48	2401	3.876576	0.750618
96	9409	1.940410	0.026729
192	37249	0.972252	0.001577

Consequently, local interpolation B-spline CAD model based on an interpolation spline cubic curve with zero second derivatives at the endpoints is used here. In the term of approximation B-spline surface, this local interpolation CAD model is determined from control points computed in software Maple and is referred to as IntSrfL. The global interpolation B-spline CAD model (referred to as IntSrfG) is modelled in Rhinoceros using the command "Surface from point grid". Both types of these interpolation surfaces are modelled for each given density.

In software Rhinoceros, using the same procedure to obtain a set of definition points, the set of verification points has been generated. The verification points are located approximately in the middle between the definition points, because this is where the interpolation B-spline surface has the largest deviation from its definition mesh [7]. To use one verification set for all three densities, the points of this set have been generated in the middle between the definition points from division 192. This verification set contains 36864 points.

The deviations (normal distances) of the verification point set from all interpolation CAD models have been obtained from Rhinoceros. An example of visual representation of the verification points deviations for the density given by the division 48 is shown in Fig. 9. Statistical evaluation for all considered densities is summarized in Table 2 (for IntSrfL models) and in Table 3 (for IntSrfG models).

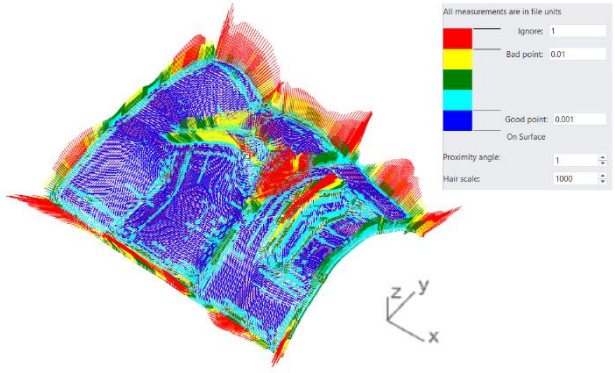


Fig. 9 *Visual representation of verification points deviation from the interpolation CAD model IntSrfL (division 48).*

It is clear that all interpolation models meet their predicted geometrical accuracy *g*, because the maximum distance between the verification points and the interpolation surface is lower than the accuracy *g* calculated by (5) (for each given density).

Table 2: *Statistical evaluation of verification points deviations from IntSrfL CAD models.*

Division [-]	48	96	192
Average distance [mm]	0.001920	0.000215	0.000025
Standard deviation [mm]	0.003358	0.000521	0.000100
Maximum distance [mm]	0.044568	0.005598	0.001448
Geom. accuracy *g* [mm]	0.750618	0.026729	0.001577

Table 3: *Statistical evaluation of verification points deviations from IntSrfG CAD models.*

Division [-]	48	96	192
Average distance [mm]	0.001219	0.000090	0.000007
Standard deviation [mm]	0.002058	0.000192	0.000017
Maximum distance [mm]	0.025128	0.002461	0.000277
Geom. accuracy *g* [mm]	0.750618	0.026729	0.001577

5. Conclusion

In this p**a**per, a method to predict geometrical accuracy of a computer-readable interpolation CAD model of a freeform surface with a given density of definition points is described and verified. The input data for the method is represented by a quadrilateral mesh of the points obtained, for example, by tactile point to point coordinate measurement of the original shape (a workpiece with freeform superficies). The geometrical accuracy of an interpolation CAD model depends not only on the density of the input points but also on the curvature of the original surface given by a minimum curvature radius. In case of the nominal CAD model of the surface being available, the minimum curvature radius can be obtained from a curvature analysis of the nominal CAD model in a suitable software. Otherwise, the minimum curvature radius can be measured by means of radius gauges or derived from the radius of cutting tool. In any case, it is necessary to emphasise that the minimum radius of the curvature is an internal (local) property of the surface in terms of differential geometry [12]. Therefore, the global shape of the surface must be taken into account in order not to overestimate the radius *r*, and consequently, the distance *d*.

For three densities of the definition points sets, the results of the proposed method were demonstrated and verified by processing the experimental data generated on a test freeform surface. Two types of interpolation B-spline CAD models were constructed (for each of the three data point set) and the estimation of geometrical accuracy was verified using a set of the verification points at suitable position. Due to the fact, that the range of normal deviations of the verification points sets from both types of the interpolation CAD models satisfied the geometrical accuracy condition, the proposed method was declared successful.

The derivation of the dependence of the interpolation surface geometrical accuracy on the maximum distance between two neighbouring definition points and the minimum curvature radius leads to a numerical solution not applicable in the technical practice. Therefore, this dependence could be performed, for instance, like a graph of geometrical accuracy *g* as a function of a maximum distance *d* (for the given radius *r*), by approximation of an appropriate amount of discrete values *g* for *d* from some given interval *I* by least-squares third degree polynomials. In this case, the estimation of geometrical accuracy *g* for any maximum distance *d* from interval *I* could be deducted from the graph.

The proposed method is useful, for example, in shape reconstruction applications and freeform surfaces inspections. The future research will be focused especially on applications in precise CAD-based freeform coordinate metrology, where the accuracy of the conformity of the measured freeform shape and the reference CAD model is essential.

6. Acknowledgment

The paper was supported by student grant SGS21/148/OHK2/3T/12: Applications of mathematical-geometric modelling in mechanical engineering from Grant Agency of CTU in Prague.

7. References

1. A. Manor, A. Fischer, *Reverse Engineering of 3D Models Based on Image Processing and 3D scanning Techniques*, (342-356, 2001)
2. Y. Liu, M. Yen, Optimized triangle mesh reconstruction from unstructured points. The visual Computer, 19:23-37, **03** (2003)
3. G. Mansour, A developed algorithm for simulation of blades to reduce the measurement points and time on coordinate measuring machine. Measurement, 54:51-57 (2014)
4. E. Savio, L. Chiffre, R. Smith, Metrology of freeform shaped parts. CIRP annals – Manufacturing technology, 56:810-835, **12** (2007)
5. L. Beiser, *Unified Optical Scanning Technology*, (John Wiley & Sons, Ltd, 2003)
6. V. Mehrad, D. Xue, P. Gu, Prediction of surface reconstruction uncerntainties for freeform surface inspection. Measurement, 46:2682-2694, **10** (2013)
7. L. Piegl, W. Tiller, *The NURBS Book*, (Springer, 1997)
8. P. Skalník, V. Zelený, I. Linkeová, Calibration of freeform standard. In Proceedings of the 15th international conference of the European society for precision engineering and technologies euspen, 147-148 (2015)
9. V. Zelený, I. Linkeová, P. Skalník, Calibrated cad model of freeform standard. In XXI IMEKO World Congress Measurement in Research and Industry, 1423-1428 (2015)
10. *International vocabulary of metrology – Basic and general and associated terms* (VIM, Standard, BIMP, 2012)
11. S. Hyde, B. W. Ninham, S. Andersson, K. Larsson, T. Landh, Z. Blum, S. Lidin, Chapter I – the mathematics of curvature, *The Language of Shape*, (Elsevier Science B. V., 1997)
12. K. Tapp, *Differential Geometry of Curves and Surfaces*, (Springer International Publishing, 2016)

Temperature field in a layered plate with local heating

Vasyl Havrysh[1,2], Liubov Koliasa[1,3], Svitlana Vozna[1,4]

[1] Lviv Polytechnic National University, Lviv, Ukraine

[2] vasyl.i.gavrysh@lpnu.ua, https:// orcid.org/ 0000-0003-3092-2279

[3] liubov.i.koliasa@lpnu.ua, https:// orcid.org/0000-0002-9690-8042

[4] svitlana.m.vozna@lpnu.ua, https:// orcid.org/0000-0002-5354-2124

Abstract: *In this paper, analytical expressions are obtained for determining the temperature distribution in a two-layer medium with local heating concentrated on the interface surface of the layers for a stable and linearly variable relative to the temperature of the thermal conductivity coefficient of the materials of the layers. Numerical calculations are given, and on this basis, the curves of temperature distribution as a function of spatial coordinates were constructed, which make it possible to analyze the temperature regimes in a two-layer plate.*

Keywords: HEAT EXCHANGE, ISOTROPIC TWO-LAYER PLATE, THERMAL CONDUCTIVITY, TEMPERATURE FIELD, HEAT-INSULATED SURFACE, PERFECT THERMAL CONTACT.

1. Introduction

Modeling of heat dissipation processes in various structures and their elements is an important area of theoretical and practical research. It is known that the elements of modern electronic devices are exposed to internal heating as a result of operation. That is why the problems of mathematical modeling of heat transfer processes are still relevant today, because the analysis of solutions of such problems is of great scientific, practical and economic importance.

Thus, the problem of developing new mathematical models for both homogeneous and inhomogeneous media, as well as the improvement of already developed mathematical models for the analysis of the process of thermal conductivity and heat transfer remains relevant.

Determination of temperature regimes in both homogeneous and inhomogeneous structures attracts the attention of many researchers [1] – [6].

The paper [7] presents isotropic gentle thin shells heated by internal heat sources, concentrated in a square and an ellipse, on the boundary surfaces of which convective heat exchange with the environment takes place. The problem of thermal conductivity is solved under conditions when the ambient temperature is constant and goes to zero at infinity. Heat sources with an intensity equal to one are placed on the middle surface, where the beginning of the coordinate system is selected. The bulk density of heat sources is described by the two-dimensional Dirac function. The behavior of the temperature field in the medium and the dependence of temperature on the distance to heat sources have been studied.

In [8] the heat exchange in a layered plate with components of different transparency connected by a thin intermediate layer under thermal irradiation from the side of a partially transparent layer was investigated. Using an effective reflection coefficient on the contact surface, approximate ratios are obtained to determine the radiation field in the mainly partially transparent layer.

An external asymptotic decomposition of the solution of the nonstationary thermal conductivity problem for a layered anisotropic plate with boundary conditions of the second kind on the front surfaces is performed. The obtained two-dimensional differential equations are analyzed and the asymptotic properties of the solutions of the problem are investigated. Estimates of the accuracy with which the temperature distribution outside the boundary layer of the plate is considered to be a piecewise linear or piecewise quadratic function in terms of thickness are obtained [9]. In works [10], [11] the existing and new approaches to creation of mathematical models of the analysis of heat exchange between piece-homogeneous designs and environment are improved. In [12], [13] the general equations of thermal conductivity for inhomogeneous media are given.

A review of the main literature sources showed that the models that operate under intense temperature disturbances caused by locally concentrated heat sources remained unexplored and undeveloped.

The aim of the research is to develop a mathematical model for the analysis of heat exchange of a two-layer plate with the environment, which is heated by an internal point heat source concentrated on the conjugation surfaces of the layers. The created mathematical model will allow to increase the accuracy of heat exchange determination between layered structures and the environment, which will further affect the efficiency of digital technology device design methods.

2. Prerequisites and means for solving the problem

Consider an isotropic with respect to thermophysical parameters two-layer plate whose thickness is 2δ with heat-insulated facial surfaces $|z|=\delta$, which consists of two heterogeneous layers of different geometrical (width) and of different thermos-physical (heat conduction coefficient) parameters and it is referred to the Cartesian rectangular system of coordinates (x,y,z). The point heat source with power $q_0 = const$ is concentrated at the origin of the Cartesian rectangular system of coordinates. The origin of which is located at the conjugation surface $K_0 = \{(x,0,z): |x|<\infty, |z|\le\delta\}$. On this surface there is an ideal heat contact $t_1(x,y) = t_2(x,y)$, $\lambda_1(t_1)\frac{\partial t_1(x,y)}{\partial y} = \lambda_2(t_2)\frac{\partial t_2(x,y)}{\partial y}$ for $y=0$ (1 - for the first layer of the plate, 2 - for the second layer of the plate). On the boundary surfaces $K_1 = \{(x,-y_1,z): |x|<\infty, |z|\le\delta\}$ and $K_2 = \{(x,y_2,z): |x|<\infty, |z|\le\delta\}$ of the plate, the conditions of convective heat exchange with the environment are given in accordance with Newton's law (Fig. 1).

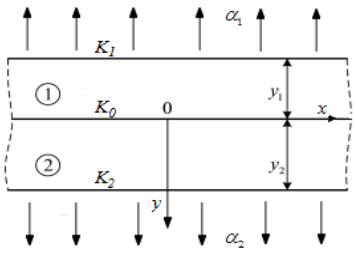


Fig. 1: Cross section of an isotropic plate with heat transfer plane z=0.

In the given structure it is necessary to determine the distribution of temperature $t(x,y)$ with respect to space coordinates is determined by means of solving the non-linear equation of heat conduction [12], [13]

(1) $$\lambda(t,y)\frac{\partial^2 t}{\partial x^2}+\frac{\partial}{\partial y}[\lambda(t,y)\frac{\partial t}{\partial y}]=-q_0\delta(x,y)$$

with a boundary conditions $t(x,y)\Big|_{|x|\to\infty}=t_c$,

$$\lambda_1\frac{\partial t(x,y)}{\partial y}\Big|_{y=-y_1}=\alpha_1(t-t_c),$$

(2) $$\lambda_2\frac{\partial t(x,y)}{\partial y}\Big|_{y=y_2}=-\alpha_2(t-t_c),$$

where $\lambda(y)$ is the coefficient of heat conductivity of the non-homogeneous plate,

(3) $$\lambda(y)=\lambda_1+[\lambda_2-\lambda_1]S_+(y);$$

$\lambda_1(t)$ and $\lambda_2(t)$ are the coefficients of heat conductivity of the materials of the 1-st and 2-nd layers of the plate respectively; t_c is ambient temperature; α_1 and α_2 are heat transfer coefficients from surfaces K_1 and K_2 respectively; $S_+(y)$ is the asymmetric unit functions [14];

$$S_+(\zeta)=\begin{cases}1, & \zeta>0,\\ 0, & \zeta\le 0\end{cases}$$ is the symmetric unit functions;

$\delta(\zeta)=\frac{dS(\zeta)}{d\zeta}$ is delta function of Dirack.

Introduce function

(4) $$T(x,y)=\lambda(y)\theta(x,y)$$

and differentiate it by variables x and y considering expression for the coefficient of thermal conductivity $\lambda(y)$ (3). As a result, we obtain $\lambda(y)\frac{\partial\theta}{\partial y}=\frac{\partial T}{\partial y}-(\lambda_2-\lambda_1)\theta|_{y=0}\delta_+(y);$

(5) $$\lambda(y)\frac{\partial\theta}{\partial x}=\frac{\partial T}{\partial x},$$

where $\theta(x,y)=t(x,y)-t_c$ is the excess temperature;

$\delta_+(\zeta)=\frac{dS_+(\zeta)}{d\zeta}$ is the asymmetrical Dirac delta functions [14].

Substituting expressions (5) in relationship (1), we arrive at a differential equation with partial derivatives with singular coefficients:

(6) $$\Delta T-(\lambda_2-\lambda_1)\theta\big|_{y=0}\delta'_+(y)=-q_0\delta(x,y),$$

where Δ is the Laplace operator in the Cartesian rectangular coordinate system, $\Delta=\frac{\partial^2}{\partial x^2}+\frac{\partial^2}{\partial y^2}$.

Therefore, the required temperature field in the given system is completely determined by equation (6) with boundary conditions (2).

3. Solution of the examined problem

Let us apply the integral Fourier transform by the x coordinate to equation (6) and boundary conditions (2) taking into consideration relationship (4), we obtain the differential equation with constant coefficients

(7) $$\frac{d^2\overline{T}}{dy^2}-\xi^2\overline{T}=(\lambda_2-\lambda_1)\overline{\theta}\big|_{y=0}\delta'_+(y)-\frac{q_0}{\sqrt{2\pi}}\delta(y)$$

with boundary conditions

$$\frac{d\overline{T}}{dy}\Big|_{y=-y_1}=\frac{\alpha_1}{\lambda_1}\overline{T}\big|_{y=-y_1},\ \frac{d\overline{T}}{dy}\Big|_{y=y_2}=-\frac{\alpha_2}{\lambda_2}\overline{T}\big|_{y=y_2},$$

where $\overline{T}(y)$ is transformant function $T(x,y)$, $\overline{T}(y)=\frac{1}{\sqrt{2\pi}}\int_{-\infty}^{\infty}e^{i\xi x}T(x,y)d\xi$; ξ is the parameter of the integral Fourier transform, $i^2=-1$.

We obtain the general solution of equation (7) using the method of variation of constants in the form:

(8) $$\overline{T}(y)=c_1e^{\xi y}+c_2e^{-\xi y}+(\lambda_2-\lambda_1)\overline{\theta}\big|_{y=0}ch\xi yS_+(y)-\frac{q_0}{\xi\sqrt{2\pi}}sh\xi yS(y),$$

where c_1, c_2 are integration constants.

The value $\overline{\theta}\big|_{y=0}$ is determined from expression (9) in the form $\overline{\theta}\big|_{y=0}=\frac{c_1+c_2}{\lambda_1}$. Using boundary conditions (8) to determine the integration constants, we obtain the solution of problem (7), (8), namely

(9) $$\overline{T}(y)=\frac{q_0}{\xi\sqrt{2\pi}}\left[\frac{1}{D}\left(\overline{T}_1(y)+\overline{T}_2(y)\overline{T}_3(y)\right)-sh\xi yS(y)\right],$$

where $\overline{T}_1(y)=ch\xi(y+y_1)+\frac{\alpha_1}{\lambda_1\xi}sh\xi(y+y_1);$

$$\overline{T}_2(y)=(K_\lambda-1)\left(ch\xi y_1+\frac{\alpha_1}{\lambda_1\xi}sh\xi y_1\right)ch\xi yS_+(y));$$

$$\overline{T}_3(y)=ch\xi y_2+\frac{\alpha_2}{\lambda_2\xi}sh\xi y_2;$$

$$\overline{T}_4(y)=ch\xi(y+y_1)+(K_\lambda-1)ch\xi y_1ch\xi yS_+(y);$$

$$D=(K_\lambda-1)\left(ch\xi y_1+\frac{\alpha_1}{\lambda_1\xi}sh\xi y_1\right)\left(sh\xi y_2+\frac{\alpha_2}{\lambda_2\xi}ch\xi y_2\right)+D_1;$$

$$D_1=\left(1+\frac{\alpha_1\alpha_2}{\lambda_1\lambda_2\xi^2}\right)sh\xi(y_1+y_2)+\frac{1}{\xi}\left(\frac{\alpha_1}{\lambda_1}+\frac{\alpha_2}{\lambda_2}\right)ch\xi(y_1+y_2),$$

$$D_2=sh\xi(y_1+y_2)+(K_\lambda-1)sh\xi y_2ch\xi y_1,$$

$K_\lambda=\lambda_2/\lambda_1$ is a coefficient that characterizes the relative thermal conductivity of the plate layers.

Having applying the inverse Fourier integral transformation to the relationship (10), we obtain the solution of problem (1), (2) in the form

(10) $$T(x,y)=\frac{q_0}{\pi}\int_0^\infty\frac{\cos\xi x}{\xi}\left[\frac{1}{\Delta}\left(\overline{T}_1(y)+\overline{T}_2(y)\overline{T}_3(y)\right)-sh\xi yS(y)\right]d\xi.$$

Therefore, the searched temperature field in the two-layer plate, which is due to the point source of heat concentrated on the conjugation surfaces of the plate layers, is expressed by formula (11), from which we obtain the value of temperature at any point of the given structure.

In the partial case, for boundary conditions of the second kind

(11) $$t\,|_{|x|\to\infty}=t_c,\ \frac{\partial t}{\partial y}\Big|_{y=-y_1}=\frac{\partial t}{\partial y}\Big|_{y=y_2}=0$$

we obtain the solution of problem (1), (12) in the form

(12) $$T(x,y)=\frac{q_0}{\pi}\int_0^\infty\frac{\cos\xi x}{\xi}\left[\frac{ch\xi y_2}{D_2}\overline{T}_4(y)-sh\xi yS(y)\right]d\xi.$$

Nonlinear mathematical model. Let us consider the case when a two-layer plate is thermosensitive (thermophysical parameters

depend on temperature). The heat equation and boundary conditions are written in the form

$$\lambda(t,y)\frac{\partial^2 t}{\partial x^2}+\frac{\partial}{\partial y}[\lambda(t,y)\frac{\partial t}{\partial y}]=-q_0\delta(x,y). \quad (13)$$

$$t(x,y)\Big|_{|x|\to\infty}=0,\frac{\partial t(x,y)}{\partial y}\Big|_{y=-y_1}=\frac{\partial t(x,y)}{\partial y}\Big|_{y=y_2}=0, \quad (14)$$

Consider the linearizing function

$$t(x,y)\Big|_{|x|\to\infty}=0,\frac{\partial t(x,y)}{\partial y}\Big|_{y=-y_1}=\frac{\partial t(x,y)}{\partial y}\Big|_{y=y_2}=0, \quad (15)$$

differentiating which by the variables *x* and *y*, we obtain:

$$\begin{aligned}&\lambda(t,y)\frac{\partial t(x,y)}{\partial x}=\frac{\partial \vartheta(x,y)}{\partial x}+\\&+\left\{\left[\lambda_2(t)-\lambda_1(t)\right]\frac{\partial t(x,y)}{\partial x}\right\}\Big|_{y=0}S_-(y),\\&\lambda(t,y)\frac{\partial t(x,y)}{\partial y}=\frac{\partial \vartheta(x,y)}{\partial y}.\end{aligned} \quad (16)$$

Taking into account expressions (17), the equation (14) will take the following form:

$$\Delta\vartheta+S_-(y)\frac{\partial}{\partial x}\left\{\left[\left(\lambda_2(t_{j+1})-\lambda_1(t_{j+1})\right)\frac{\partial t}{\partial x}\right]\Big|_{y=0}\right\}=-q_0\delta(x,y). \quad (17)$$

We write the boundary conditions using relationship (16) as follows:

$$\vartheta(x,y)\Big|_{|x|\to\infty}=0,\frac{\partial \vartheta(x,y)}{\partial y}\Big|_{y=-y_1}=\frac{\partial \vartheta(x,y)}{\partial y}\Big|_{y=y_2}=0. \quad (18)$$

Linearizing function (16) made it possible to reduce the nonlinear equation of heat conduction (14) to a partially linearized equation (18) with discontinuous coefficients and completely linearized boundary conditions (19).

4. Results and discussion

Numerical-analytical solution. We approximate the function *t(x,0)* by the expression

$$t(x,0)=t_1+\sum_{j=1}^{n-1}(t_{j+1}-t_j)S_-(x-x_j), \quad (19)$$

where $x_j \in]-x_*;\ x_*[;\ x_1\le x_2\le\ldots x_{n-1};$ n is the number of subintervals of the interval $]-x_*;\ x_*[;$ $t_j\ (j=\overline{1,n})$ are unknown approximately values of temperature; x_* is the value of the coordinate *x* in which temperature is practically to zero (determined from the equal corresponding linear boundary condition).

Let us substitute the relationships (20) into (18) and obtain the partial linear differential equation for determination of the linearizing functionï $\vartheta(x,y)$

$$\begin{aligned}&\Delta\vartheta=-S_-(y)\sum_{j=1}^{n-1}\left[\lambda_2(t_{j+1})-\lambda_1(t_{j+1})\right](t_{j-1}-t_j)\delta'(x-x_j)-\\&-q_0\delta(x,y).\end{aligned} \quad (20)$$

Having applied Fourier integral transformation with respect to the spatial coordinate x for the equation (21) and the boundary value problem (19), we obtain the ordinary differential equation with constant coefficients

$$\begin{aligned}&\frac{d^2\bar{\vartheta}}{dy^2}-\xi^2\bar{\vartheta}=\\&=\frac{1}{\sqrt{2\pi}}\left\{i\xi S_-(y)\sum_{j=1}^{n-1}\left[\lambda_2(t_{j+1})-\lambda_1(t_{j+1})\right](t_{j+1}-t_j)e^{i\xi x_j}-q_0\delta(y)\right\}\end{aligned} \quad (21)$$

with the boundary conditions

$$\frac{d\bar{\vartheta}(y)}{dy}\Big|_{y=-y_1}=\frac{d\bar{\vartheta}(y)}{dy}\Big|_{y=y_2}=0, \quad (22)$$

where $\bar{\vartheta}(y)=\frac{1}{\sqrt{2\pi}}\int_{-\infty}^{\infty}e^{i\xi x}\vartheta(x,y)dx$ – transforming function $\vartheta(x,y)$.

Having solved the boundary value problem (22), (23) and having applied the inverse Fourier integral transformation to the obtained solution, we obtain:

$$\begin{aligned}&\vartheta(x,y)=-\frac{1}{\pi}\int_0^{\infty}\frac{1}{\xi}\left\{\left[\frac{ch\xi(y+y_1)}{sh\xi(y_1+y_2)}sh\xi y_2-\right.\right.\\&-\left.(ch\xi y-1)S(y)\right]\sum_{j=1}^{n-1}\sin\xi(x-x_j)\left(t_{j+1}-t_j\right)\times\left[\left(\lambda_2(t_{j+1})-\lambda_1(t_{j+1})\right)\right]-\\&\left.-q_0\cos\xi x\times\left(\frac{ch\xi(y+y_1)}{sh\xi(y_1+y_2)}ch\xi y_2-sh\xi yS(y)\right)\right\}d\xi.\end{aligned} \quad (23)$$

Substituting the expressions for the temperature dependence of the thermal conductivity of materials for each of the layers of the plate into relationships (16), (24), after some transformations we obtain a system of nonlinear equations for determining the unknown approximating temperature values $t_j\ (j=\overline{1,n})$. The searched temperature field for the reduced structure is determined using the obtained nonlinear equation using ratios (16), (24), after substituting in them specific turns of the dependence of the thermal conductivity of structural materials on temperature.

A particular example and analysis of the results obtained. To solve many practical problems, the following dependence of the thermal conductivity coefficient on temperature is used [12, 13]:

$$\lambda_s=\lambda_s^0(1-k_st), \quad (24)$$

where λ_s^0, k_s – reference and temperature coefficients of thermal conductivity of the materials of the layers of the (s=1, 2). From expressions (16), (24), we obtain formulas for determining the temperature *t(x,y)* in the domains of the first $\Omega_1=\{(x,y):|x|<\infty,-y_1\le y<0\}$ –

$$t(x,y)=\frac{1-\sqrt{1-2\frac{k_1}{\lambda_1^0}\vartheta(x,y)}}{k_1} \quad (25)$$

and the second $\Omega_2=\{(x,y):|x|<\infty,0\le y\le y_2\}$ –

$$t(x,y)=\frac{1-\sqrt{1-2\frac{k_2}{\lambda_2^0}(\vartheta(x,y)+\vartheta_1)}}{k_2} \quad (26)$$

layers of the plate.

Here $\vartheta_1=\left\{t\left[\lambda_2^0\left(1-\frac{k_2}{2}t\right)-\lambda_1^0\left(1-\frac{k_1}{2}t\right)\right]\right\}\Big|_{y=0}$.

The temperature value $t(x,0)$ is determined by the formula (26).

Formulas (26), (27) fully describe the temperature field in a thermosensitive two-layer plate.

Results of numerical calculations. A numerical analysis of the temperature $\theta(x, y)$ in a two-layer plate is performed for the following initial data: plate materials is copper ($\lambda_1 = 395$ w/(m·deg) at the temperature $t = 20\,^{\circ}$C) for the first layer and aluminum $(\lambda_2 = 207$ w/(m·deg) at the temperature $t = 27°C)$ for the second layer; $y_1 = y_2 = 1$ м; $q_0 = 200$ вт.

In the case of a nonlinear model in the temperature interval [27°C; 927°C], the aforesaid materials are described by the following dependences of coefficient of heat conductivity on temperature:

$$\lambda_1(t) = 381,62\frac{\text{W}}{\text{Km}}(1 - 0,00021\frac{1}{\text{K}}t),$$

$$\lambda_2(t) = 211,25\frac{\text{W}}{\text{Km}}(1 - 0,00076\frac{1}{\text{K}}t).$$

Numerical calculations are performed with accuracy $\varepsilon = 10^{-6}$.

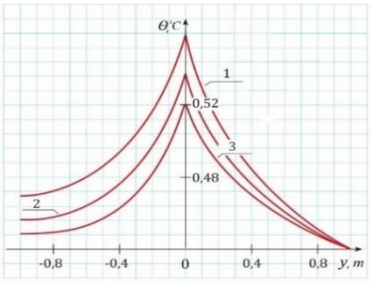


Fig. 2: The dependence of temperature $\theta(x, y)$ on the coordinate y for x = 0 and the given values of the heat transfer coefficient:

curve 1 – $\alpha_1 = \alpha_2 = 17,64$ W / (m$^2 \cdot {}^0$C);

curve 2 – $\alpha_1 = \alpha_2 = 15,74$ W / (m$^2 \cdot {}^0$C);

curve 3 – $\alpha_1 = \alpha_2 = 13,59$ W / (m$^2 \cdot {}^0$C).

The change of temperature depending on the spatial coordinate y for $x = -2$ and the given values of the heat transfer coefficient is illustrated (Fig. 2). The behavior of the curves shows that the temperature, as a function of the y coordinate, increases monotonically in the first layer of the plate and reaches its maximum value at the point (0; 0), where the point heat source is concentrated, and in the second layer of the plate it decreases monotonically. In this case, the temperature reaches the lowest values on the boundary surfaces of the plate. As can be seen from the figures, heat transfer coefficients significantly affect the temperature distribution, , and it is higher in the first layer, because the material of this layer is copper and the thermal conductivity is greater than the thermal conductivity for the second layer, the material of which is aluminum.

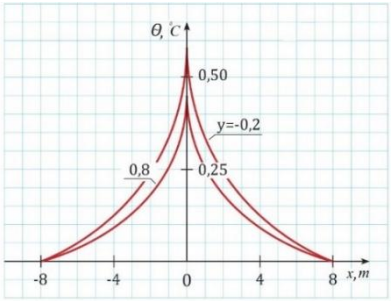


Fig. 3: The dependence of temperature $\theta(x, y)$ on the coordinate x for $\alpha_1 = \alpha_2 = 16,92$ W / (m^2 ^{0}C) and the given values of the coordinate y.

Figure 3 shows the change in temperature depending on the spatial coordinate x and the given values of the spatial coordinate y. From the behavior of the curves it is seen that the temperature, as a function of the x coordinate, is a fairly smooth and monotonic function and reaches its maximum value at the point (0; 0). In the case of an increase in the absolute value of the values of the spatial coordinate x, the temperature decreases, which indicates that the mathematical model corresponds to the real physical process.

5. Conclusion

Using generalized functions and integral Fourier transform for a two-layer plate with a point heat source and heat transfer, an analytical solution of the boundary value problem of thermal conductivity is constructed, the differential equation of which contains discontinuous and singular coefficients.

This solution is presented in the form of an improper convergent integral. Using it, an algorithm and a calculation program for determining the temperature field at an arbitrary point of a two-layer plate with a point heat source concentrated on the surface of the conjugation of layers are developed. On this basis, numerical values of the temperature field are obtained, using which graphs are plotted, which show the curves that reflect the behavior of temperature depending on the spatial coordinates and values of the heat transfer coefficient from the boundary surfaces of the plate. This makes it possible to analyze the heat exchange in nonhomogeneous layered media in terms of their heat resistance during heating and protect them from overheating, which can cause the destruction of not only individual elements but also the entire structure.

6. Acknowledgement

The obtained analytical solutions of linear and nonlinear boundary value problems of thermal conductivity for a layered medium with local heating allow the development of algorithms and software for their numerical implementation for the analysis of heat transfer in individual structural elements and nodes of digital devices with the aim of predicting their operating modes, identifying unknown parameters and increasing heat resistance, which increases their service life.

7. Literature

[1] A. Carpinteri, Thermoelastic mismatch in nonhomogeneous beams, J. Eng. Math., 61(2–4), (2008) 371–384.(A. Carpinteri, M. Paggi)

[2] N. Noda, Thermal stresses in materials with temperature-dependent properties, Appl. Mech. Rev., 44 (1991) 383-397.

[3] Y. Otao, Optimization of material composition of functionality graded plate for thermal stress relaxation using a genetic algorithm, J. Therm. Stresses, 23 (2000) 257-271.(Y. Otao, O. Tanigawa, O. Ishimaru)

[4] O. Tanigawa, Transient heat conduction and thermal stress problems of a nonhomogeneous plate with temperature-dependent material properties, J. Therm. Stresses, 19, No. 1 (1996) 77-102.(O. Tanigawa, T. Akai, R. Kawamura)_

[5] O. Tanigawa, Transient thermoelastic analysis of functionally graded plate with temperature-dependent material properties taking into account the thermal radiation, Nihon Kikai Gakkai Nenji Taikai Koen Ronbunshu, 2 (2002) 133-134.(O. Tanigawa, Y. Otao)

[6] Xu Yangian, Analysis of steady thermal stress in a ZrO2/FGM/Ti-6Al-4V composite ECBF plate with temperature-dependent material properties by NFEM, WASE Int. Conf. on Informa. Eng., 2 (2009) 433-436.(Xu Yangian, Tu Daihui)

[7] K. M. Dovbnia, Statsionarnyi teploobmin tonkykh polohykh izotropnykh obolonok, yaki znakhodiatsia pid diieiu dzherel tepla, zoseredzhenykh po dvovymirnii oblasti, Visnyk DonNU. Ser. A: Pryrodnychi nauky, №1-2 (2016) 107 -112. [In Ukrainian].(K. M. Dovbnia, O. D. Dundar)

[8] O.Turii, Neliniina kontaktno-kraiova zadacha termomekhaniky dlia oprominiuvanoi dvosharovoi plastyny, ziednanoi promizhkovym sharom, Fizyko-matematychne modeliuvannia ta informatsiini tekhnolohii, 8 (2008) 118–132. [In Ukrainian].

[9] Iu. Nemirovskii, Asimptoticheskii analiz zadachi nestatcionarnoi teploprovodnosti sloistykh anizotropnykh neodnorodnykh plastin pri granichnykh usloviiakh pervogo i tretego roda na litcevykh poverkhnostiakh. Mat. metodi ta

fiz.-mekh. polia, 50(2), (2007) 160–175. [In Russian].(Iu. Nemirovskii, A. Iankovskii)

[10] V. Havrysh, Investigation of temperature modes in thermosensitive non-uniform elements of radioelectronic devices, №3(46), (2018) 7-15. (V. Havrysh, Ya. Baranetskiy, L. Kolyasa)

[11] V. Havrysh, Determination of temperature field in thermally sensitive layered medium with inclusions, Naukovyi Visnyk NHU, №1 (2019) 94-100.(V. Havrysh, L. Kolyasa, O. Ukhanska)

[12] Ia. Podstrigach, Termouprugost tel neodnorodnoi struktury,Science, Moscow, 1984, 368 p. [In Russian].(Ia. Podstrigach, V. Lomakin, Iu. Koliano)

[13] Yu. Koliano, Metody teploprovidnosti i termopruzhnosti neodnoridnoho tila, Naukova dumka, Kyiv, 1992, 280 p. [In Russian].

[14] G. Korn, Spravochnik po matematike dlia nauchnykh rabotnikov i inzhenerov, Science, Moscow, 1977, 720 p. [In Russian].(G. Korn, T. Korn)

Modeling transient signals in power lines

Rustem Khuziashev, Igor Kuzmin, Ildar Minaev
Kazan state power engineering university, Kazan, Russia
142892@mail.ru

Abstract: *Modeling in PSCAD / EMTDS of traveling waves in a single-wire power transmission line is considered. Traveling waves of the terrestrial mode are generated at the beginning and in the middle of the line in different ways. The effects of dispersion, which lead to the dependence of the recording time of a traveling wave on the value of the registration threshold and on the distance traveled, are considered. The term of instantaneous and average speed is introduced. The values of the instantaneous speed with multiple runs of the line length drop to 250 m / μs. The average speed of a traveling wave with a single run of the line decreases by 4-6% relative to the speed of light for real thresholds of signal registration.*
Keywords*: TRAVELING WAVES, DISPERSION, INTERFERENCE, STANDING WAVE, TRANSITION SIGNAL*

1. Introduction

Emergency modes in power lines are caused by switching processes. Commutations cause the appearance of traveling waves propagating in all directions along the line. Registration of traveling waves forms the basis of the traveling wave fault location method [1]. The propagation mechanisms of traveling waves are determined by the structure of the line and are observed at different points of the line in the form of a transient signal. The most important parameter of a transient signal is its start time. The mode composition of the oscillations of the transient signal carries information about the type of commutation and the electrical parameters of the line.

The study of the propagation mechanisms of traveling waves and their practical application for high-speed protection of lines and determination of the location of fault is an urgent direction of research. Dispersion is the dominant mechanism in the propagation of traveling waves. It is expressed in a decrease in the speed of propagation of harmonic oscillations with a decrease in frequency and an increase in damping with an increase in frequency [2-4]. A method for determining the location of fauly based on the change in the shape of the leading front of a traveling wave with an increase in the distance traveled is proposed in [3].

Traveling wave fault location methods are based on determining the moment of time when a traveling wave appears in the registration place. Using the sequential application of digital filters of low and high frequency, the time instant corresponding to the maximum steepness of the leading edge of the traveling wave is determinated in [1].

2. Propagation of a voltage step caused by a switched-on power line

Connecting the line to an open-ended voltage source causes the voltage step to propagate along the length of the line. The voltage step propagation will be called the propagation of a traveling wave. The signal recorded at any point of the line is caused by the superposition of traveling waves re-reflected from inhomogeneities in the line, including its ends, and is called a transient signal (TS).

The simplest model of the formation of a transient process signal with a period equal to four times the travel time of the line length, taking into account only the reflection coefficient from the ends of the line, is considered in [5]. Oscillograms of such a signal, calculated in the PsCad package for the simplest model of a line with a length of 100 km (Fig. 1), are shown in Fig. 2 and consist of one mode vibration. The effective lifetime of the transient signal is less than the power frequency period. Therefore, the model uses a constant voltage source.

The black line in Fig. 2 depicts the trajectory of the displacement of the initial amplitude of the traveling wave of the voltage jump. At the time interval from mark 0 to mark 1, the traveling wave propagates along the line under the influence of dispersion. This is due to an increase in the frequency-dependent argument of the exponential dependence of the attenuation coefficient of the high-frequency component of the spectrum of the voltage jump signal [2]. Visually manifests itself in an increase in the duration of the leading edge of the signal. At the end of the line labeled 1, the discontinuity is reflected as a line break with a reflection coefficient of "+1" [5]. The superposition of the incident and reflected traveling waves causes an increase in the amplitude of TS, which is the result of the interference of the incident and reflected traveling voltage waves.

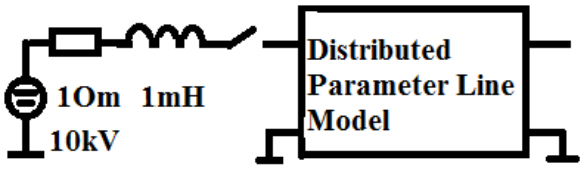


Fig. 1 *Signal "Voltage step"generation circuit at the beginning of the line.*

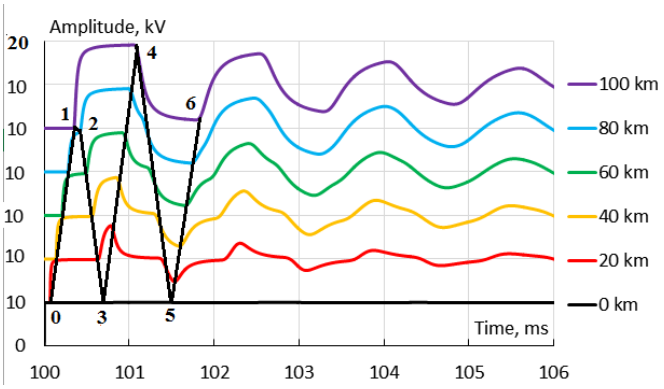


Fig. 2 *Transient signals at different distances from the beginning of the line.*

In the time interval from mark 1 to mark 2 and further to mark 3, the traveling voltage wave adds up (interferes) with the continuation of the traveling wave propagating towards the end of the line. The traveling voltage wave having reached the beginning of the line (mark 3) is reflected with the coefficient "-1" [Ionke], as from an inhomogeneity with a low transverse resistance. Visually, the traveling wave at the beginning of the line is not recorded. This is due to the presence at the beginning of the line of a powerful voltage source with a low internal resistance, which is not disturbed by the lower power of the traveling wave.

A traveling wave of negative polarity re-reflected from the beginning of the line is superimposed on its continuing tails. The propagation of this traveling wave is clearly visible in the resulting signal of the transient process from mark 3 to mark 4 (Fig. 2). At the end of the line, a traveling wave of a voltage jump of negative polarity is reflected for the second time with a reflection coefficient of "+1". Its propagation continues from mark 4 to mark 5 to the beginning of the line. At mark 5, one period of oscillations ends, recorded at all points of the line.

A traveling wave of a voltage jump is influenced by all mechanisms affecting the propagation of waves in lines - dispersion, reflection from transverse inhomogeneity, interference of re-reflected signals. The form of oscillations asymptotically, with an increase in the lifetime of the SPP and the multiplicity of the path length of the line, tend to sinusoidal.

The leading edge of a traveling wave is subject to dispersion, which visually manifests itself in a decrease in its steepness. The steepness of the leading edge is a determining factor in the accuracy of the waveform OMP method. Table 1 shows the space-time characteristics of the leading edge.

Table 1: Space-temporal characteristics of the leading edge.

Parameter \Distance, km	20	40	60	80	100
Trun[μs]	67	133	199	265	331
Aini [kV]	7,4*E-4	5,5*E-8	4*E-12	3*E-16	4,5*E-20
Vini[km/ μs]	0,298507	0,300752	0,301508	0,301887	0,302115
T_A1% [μs]	68	138	208	279	350
T_A5% [μs]	69	139	210	282	354
T_A10% [μs]	70	141	212	285	358
T_A90% [μs]	94	192	296	403	516
V_A1% [km/μs]	0,29411	0,28985	0,28846	0,28673	0,28571
V_A5% [km/μs]	0,28985	0,28777	0,28571	0,28368	0,28248
V_A10% [km/μs]	0,28571	0,28368	0,28301	0,28070	0,27933
Slope [μs/km]	1,2	1,275	1,4	1,48	1,58

The Trun time is the duration of the propagation of the initial high-frequency precursor of the traveling wave corresponds to the speed of light Vini with the calculation error in the Pscad package (Table 1). The initial high-frequency traveling wave precursor has an extremely small amplitude Aini. An increase in the duration of the leading edge at levels of 10% -90% of the maximum signal amplitude from the distance traveled corresponds to a decrease in the slope at Slope = 1.2-1.6 μs for each km traveled. The duration of the leading edge of the traveling wave is 158 μs when the line passes 100 km.

The time T_A1% of the first run of the traveling voltage wave from the beginning to the end of the line, which can be recorded by hardware methods, taking into account the real signal-to-noise ratio of 40 dB, is 350 μs (Table 1). This corresponds to the apparent speed V_A1% of propagation of a traveling wave of 286 m / μs, which is 5% less than the speed of light (Fig. 3). A similar value of the propagation speed of a traveling wave at 20 km is 294 m / μs, or 2% less than the speed of light. Accordingly, when using the average experimentally determined value of the signal propagation velocity, the error in determining the location of the signal origin is several percent of the line length.

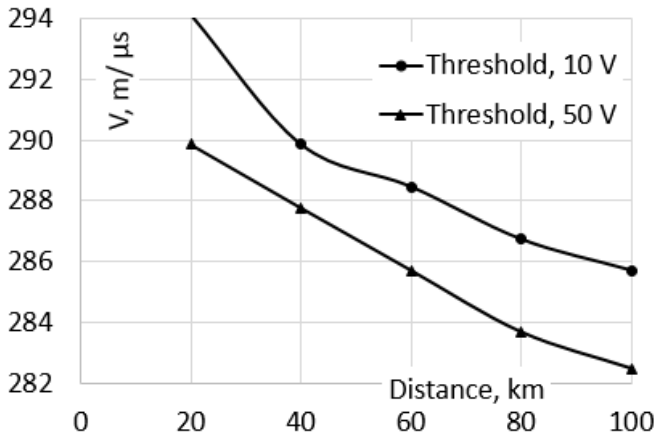


Fig. 3 *The recorded average velocity of propagation of the traveling voltage wave of the terrestrial mode at different distances from the beginning of the line.*

The half-period of the formed free oscillations is calculated from the time of intersection of the instantaneous amplitudes of the signals of the steady-state voltage of 10 kV (Fig. 2). The half-period of oscillations asymptotically, with an increase in the number of multiple reflections of the traveling wave from the ends of the line, tend to the steady-state value of 795 μs (Fig. 4). The steady-state half-cycle is set faster at the far end of the line. The steady-state oscillations are in phase with each other at any point of the line. We assume that the period of free oscillations is due to the fourfold run of the line length.

The single line wave contains only the ground wave, which corresponds to the zero mode for the three phase line. The speed of propagation of oscillations is calculated as 200 km / 795 μs = 252 m / μs. The speed corresponds to a fixed frequency of 629 Hz of steady free harmonic oscillations for the earth wave in [Smirnov] [KhRG]. This fixed speed is much lower than the average and instantaneous speeds on the first 100 km of the line (Fig. 3), which correspond to the higher frequency components of the earth wave. Thus, a standing wave mode is formed in the line in Fig. 1 at a frequency for which the line represents a quarter-wave segment. The beginning of the line corresponds to the node of the standing wave, and the end of the line corresponds to the antinode.

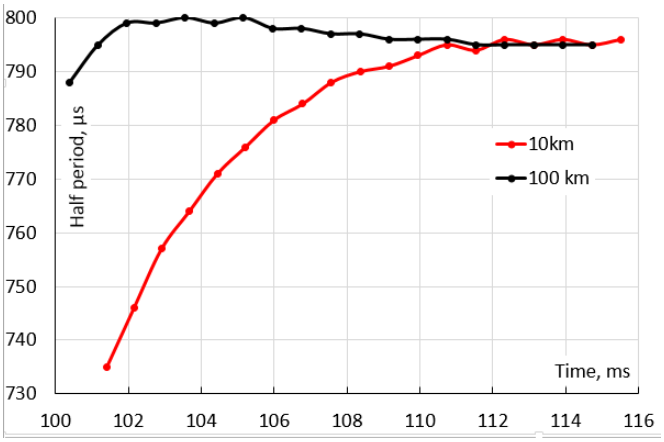


Fig. 4 *Dependence of the duration of half-periods of damped oscillations of the signal of the transient process on the time of its existence at different distances from the beginning of the line.*

3. Voltage step propagation when half line is turned on

Let's move the switching key to the middle of the line (Fig. 5). Signal oscillograms are shown in Fig. 2 and fig. 3. The generated voltage surges of different polarity propagate in opposite directions with the paths marked in Fig. 3. The number of mode oscillations in the first half of the line is two. The number of mode vibrations in

the second half of the line is one. This fact can be used for additional identification of the switching point.

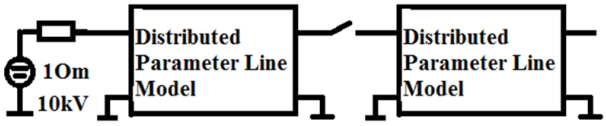


Fig. 4 *Signal "Voltage step" generation circuit in the middle of the line.*

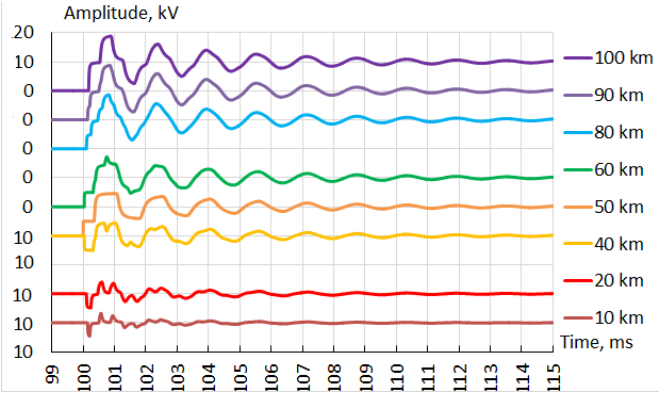


Fig. 5 *Transient signals at different distances from the beginning of the line.*

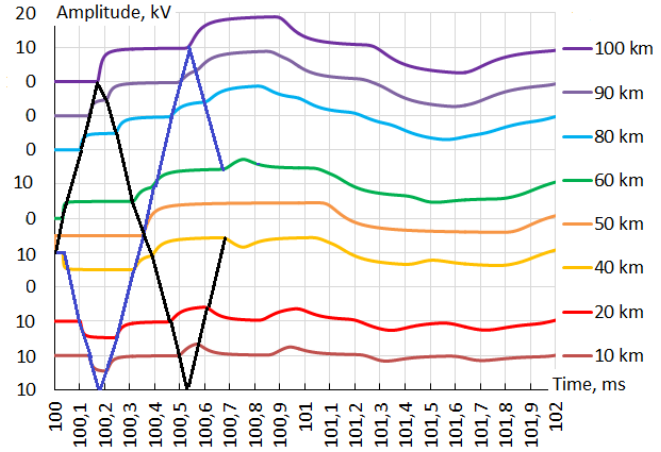


Fig. 6 *The trajectory of a traveling wave at different distances from the beginning of the line.*

4. Propagation of a voltage pulse caused by a charge capacitance

The mechanism of voltage jump propagation along the line considered in the previous section is registered experimentally. Consider the propagation of a voltage pulse generated in the line model when a capacitor is connected (Fig. 7). This circuit is the simplest model for a single-phase earth fault (SPEF) in isolated neutral distribution networks. Figure 8 shows the oscillograms of the TS recorded at different points of the line. The multimode nature of SPEF is well manifested. There are low-frequency oscillations in phase at all points of the line and high-frequency oscillations of different frequency in the first and second half of the line. The decay time constant of high-frequency modes is significantly less than the analogous value for the low-frequency mode.

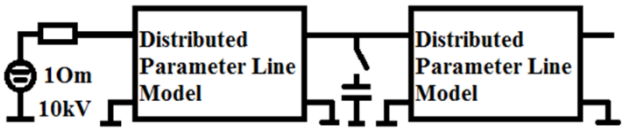


Fig. 7 *Signal "Soliton" generation circuit in the middle of the line.*

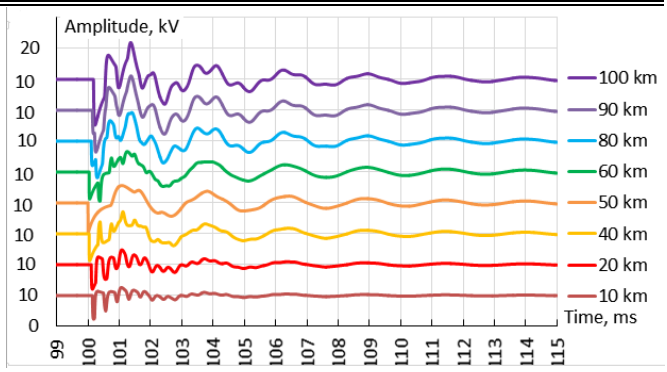


Fig. 8 *Transient signals for "Soliton" generation circuit in the middle of the line.*

Let us consider the mechanisms affecting the propagation of the leading front of the traveling wave according to Fig. 9. A traveling wave arises at the point marked with the mark 0 due to the closure of its electrical potential to ground through an uncharged capacitor. This causes a large jump in the capacitor charging current and a corresponding jump in the voltage dip. The traveling wave of a voltage dip surge propagates in opposite directions to the beginning and to the end of the line. Upon reaching the beginning of the line at the point marked 1, the traveling wave is reflected with a reflection coefficient of "-1". The reflected traveling wave is superimposed on the continuation of the traveling wave and generates the first burst of the emerging high-frequency TS mode.

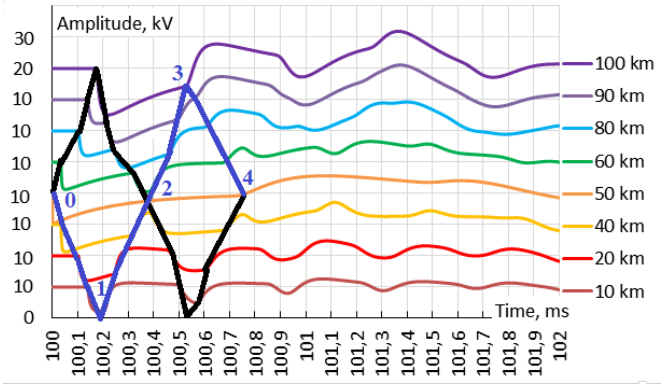


Fig. 9 *The trajectory of a traveling wave at different distances from the beginning of the line.*

A similar traveling wave propagating to the end of the line is reflected from its open end with a reflection coefficient of "+1". The traveling wave reflected from the end is in phase superimposed on the continuation of the traveling wave. A distorted rise front of the first burst of the emerging high-frequency TS mode is formed, the instantaneous amplitude of which goes over to the negative half-plane.

At the point marked 2, the traveling waves of antiphase polarities of the traveling waves are mutually eliminated both in amplitude and in synchronous time position. At the point marked 2, the unperturbed process of charging the capacitor continues according to the exponential law. At the point marked 3, the traveling wave is reflected with the reflection coefficient "+1" and is superimposed on the continuation of the traveling wave. The trailing edge of the first pulse of the emerging high-frequency TS mode is formed. At the point marked 4, the signals of the slowly changing process of charging the capacitor in the middle of the line and the one reflected from the beginning and end of the line are superimposed.

The period of steady-state free harmonic oscillations in the presence of inhomogeneity (Fig. 8) is higher than in a homogeneous line (Fig. 2 and Fig. 5). The inhomogeneity in the form of a transverse container increases the effective line length. Fig. 5 and

Fig. 6 well illustrate the twofold difference between the periods of oscillations of high-frequency modes on the two halves of the line. This fact can be used to further identify the location of damage.

5. Conclusions

Based on the results of modeling the propagation of traveling waves of the terrestrial voltage mode, it is shown that the dispersion of the leading edge of the traveling voltage wave leads to an underestimation of the recorded propagation velocity of traveling waves. The amount of underestimation is proportional to the distance traveled, depends on the registration threshold and is 0.07% of the speed of light for each km traveled for a uniform line. With the propagation of a traveling wave in an inhomogeneous line, the value of the velocity underestimation increases. Accordingly, when using the average experimentally determined value of the signal propagation velocity, the error in determining the location of the signal origin is several percent of the line length. The interference of traveling waves re-reflected from the ends of the line forms a standing wave of free oscillations at a quarter-wavelength of the line. The simulated waveforms of the transient process illustrate the possibility of determining both the type of switching and its location outside or inside the observed zone of the wave method complex for determining the fault location.

6. References

1. E.O. Schweitzer, A. Guzmán, M.V. Mynam,I. at al, 67th annual conference for protective relay engineers (pp. 95-110), (2014)
2. R.G.Huzyashev, S.M.Tukaev, I.L.Kuzmin, Energy safety and Energy-Economy, 6 (2018)
3. K.Saleh, Ph.D. dissertation, Dept. Elect. Comput. Eng., Univ. Waterloo, Waterloo, ON, Canada, (2017)
4. K.Hashemi, Transmission Line Analysis, (2016). Available: http://alignment.hep.brandeis.edu/Lab/XLine/XLine.html
5. G.V.Zevece, P.A.Ionkin, A.V. Netushil, S.V. Strakhov, *Fundamentals of the Theory of Circuits* (Moscov, 1989)
6. A.N.Smirnov, Ph.D. dissertation, Ivanovo, Russia, (2015)

Validation MAGMA model of welding process

Deyan Gradinarov[1], Georgi Georgiev[1]
Institute of Metal Science, Equipment and Technology with Hydroaerodynamic Center at Bulgarian Academy of Sciences[1]
dgradinarov@ims.bas.bg

Abstract: *It is presented comparison between captured and simulated temperatures in specific points of welding process and simulation model made with MAGMA software.*
Keywords*: MAGMA SOFTWARE, SIMULATION MODEL, WELDING PROCESS*

1. Introduction

Welding process is performed under Welding procedures (WP) in which strictly are defined the welding equipment and parameters. Welding joint quality is determined by following the welding parameters by the operator of the welding process. Variations from set it the welding procedures parameters – welding current, voltage speed, initial heating of the welded elements cause lowering the quality.

Deviation form set in the welding procedure parameters may occur by various reasons – in the equipment, in the materials and in the operator of the process. Some of those lowering welded joint quality reasons may occur during the process and some may be appear and disappear periodically during the process.

For lowering the impact on welding process and welded joints quality of such occurrences in the welding process has to be inserted quality control in real time. Such control is performed by capturing welding parameters such as welding current, voltage, speed or indirect indications as capturing temperature in one or more specific points of interest.

Physical application on welding current and voltage with defined speed heats the welded elements equally in equal other conditions and welding environment. For those reasons temperature control is applicable and used. Temperature control may be contact – mostly by thermocouples placed next to the welding joint or contactless – by pyrometers capturing temperatures focused next to the welding joint.

For better results of temperature control of the welding process thermocouples of the contact measurement and focusing the pyrometer have to be as close as possible to the trajectory of the welding torch along over the welding joint.

Unfortunately, thermocouples cannot be placed too close to the welding arc because of two reasons – the arc itself will damage or destroy the thermocouple and with this will malfunction the temperature capturing system; and melting basin next to the arc will shift or move the thermocouple. This can result in welding the thermocouple into the welding joint making welded detail unusable.

Emitted infrared light will interfere with pyrometer measurement causing false temperature result. In the case of pyrometer temperature measurement, the operator of the process or the welding torch may cause shade obstructing in visibility by the pyrometer. This has to be taken in advance to prevent interruption of the measurement[1].

Better understanding on temperature field and temperature behavior in specific point in the welding process gives computer modelling of the process[2,3]. Whit this method of analysis experimenters could expect with high probability temperature behavior of the process at the exact parameters. Computer models are validated with comparison of simulated results with experimental.

2. Validation of the model

Model of the welding process is created with MAGMA software. Validation of the model is made by comparing experimental and simulated temperature curves in 8 points.

The experimental set up consists of welding torch, which is mounted on mechanical grip. The mechanical grip fixes the torch in one position and removes fluctuations from welder's movements. The mechanical grip is mounted on welding tractor, which moves along and over the welded elements with constant speed. Welded elements are placed on welding table. Next to the welding table are placed the power source that feeds the torch and gas bottle that protects the joint. Temperature of the process is measured with 8-channel contact thermometer Spider 8. K type thermocouples are connected to the Spider 8 and set in 8 point next the welding joint. Thermocouples are welded to the welded elements. The Spider 8 is connected to the laptop with UBS cable. Temperature is captured by Spider 8 with software Catman.

Contact temperature is measured simultaneously in 6 points (from 3 to 8) placed in a row with distance of 1mm from each other starting at 3mm from the welding torch trajectory to 8mm away from it as shown on Fig.1.

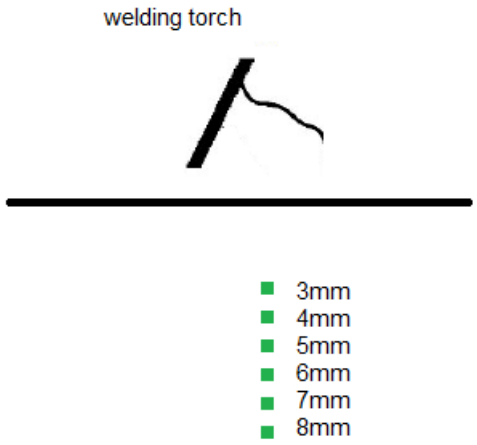


Fig. 1 *Diagram of placement of the thermocouples.*

The set up functionality is verified with experiment with the following parameters:

- welding current – 210A
- welding volatage – 25V;
- η of the welding source – 0,8;
- welding power – 4200J/s;
- welding speed – 50cm/min;
- welding steel plates 50x5x200mm.

3. Results

Results of thermocouples form point 3 (3mm) to point 8 (8mm) are shown on Fig.2.

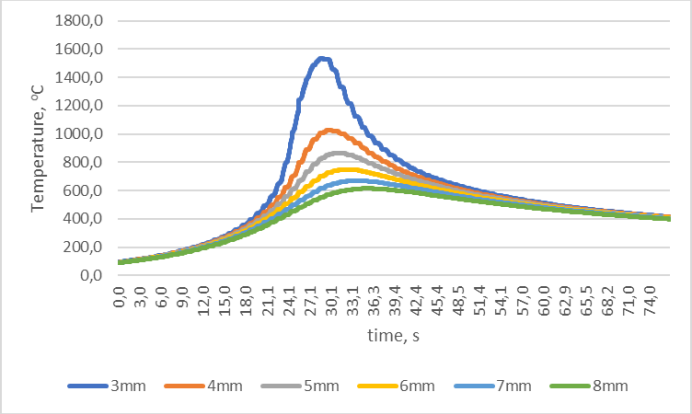


Fig. 2 *Temperature curves from thermocouple 3 (3mm) to thermocouple 8 (8mm).*

Results of simulation model form point 3 (3mm) to point 8 (8mm) are shown on Fig.3.

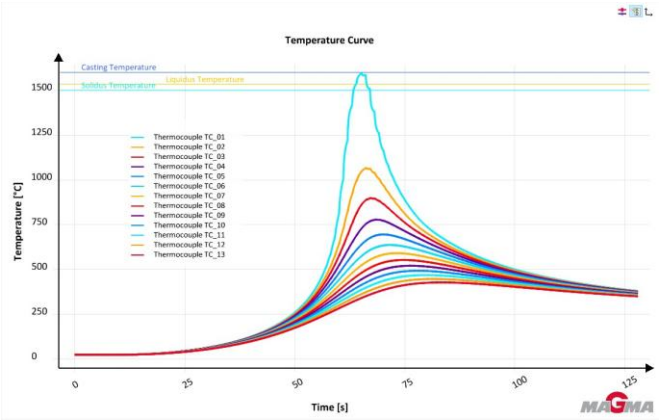


Fig. 3 *Simulated temperature curves from point 3 (3mm) to point 8 (8mm).*

Difference between measured and simulated temperature form point 3 (3mm) to point 8 (8mm) are shown on Fig.4.

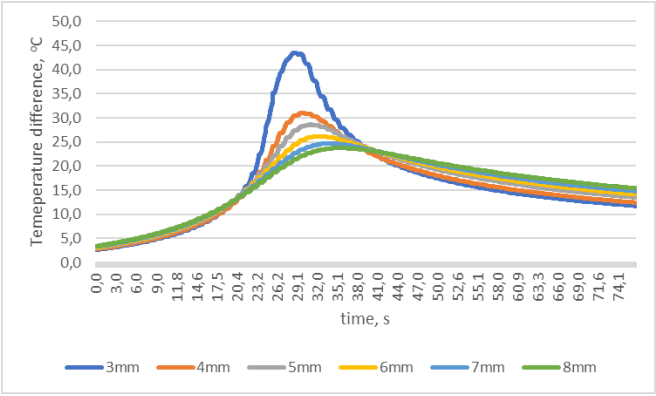


Fig. 4 *Difference between measured and simulated temperature from point 3 (3mm) to point 8 (8mm).*

Comparison between simulated and measured temperatures a very similar 3-5% difference. This gives reason to consider that the created with MAGMA model is functioning properly.

4. Conclusions

Comparison between simulated and measured temperatures a very similar 3-5% difference. This gives reason to consider that the created with MAGMA model is functioning properly.

The model could be adjusted to other elements to be welded, e.g. cylindrical to plate or cylindrical to cylindrical.

Acknowledgments

This work was made possible by a project KP-06-N37/31, funded by the NSF.

All equipment and experimental units used in this work was funded by the European Regional Development Fund within the OP "Science and Education for Smart Growth 2014 - 2020", project CoE "National center of mechatronics and clean technologies", № BG05M2OP001-1.001-0008-C08

5. *References*

1. D. Gradinarov, Yu. Bijev, I, Atanasov, St. Todorov "Algorithm for automatic calibration of pirs type IL", NDT days 2015, pp 131-133, ISSN 1310-3946
2. D. Gradinarov, Yu. Bijev, St. Todorov, "Simulation model of cross-wired EES process", NDT days 2017, pp 279-281, ISSN 1310-3946
3. G. Georgiev, Pl. Tashev, Ya. Lukarski, D. Gradinarov, "Mathematical model of temperature field at resistance welding", Engineering sciences, 2015, 1, pp. 42-51, ISSN 1312-5702

Investigation of bending strength and modulus of elasticity of a new type of black locust plywood for construction

Asen Hristov[1*], Valerii Naidenov[1], Lilyana Koleva[2]

Institute of Mechanics, Bulgarian Academy of Sciences, Bulgaria[1]
University of Chemical Technology and Metallurgy, Bulgaria[2]

[*]a.n.hristov@abv.bg

Abstract: *The mechanical properties bending strength and modulus of elasticity in bending of a new type plywood for construction, based on black locust wood, have been investigated in relationship with the bonding technological factors. The experimental investigation is based on an optimal composite design with four control factors – temperature, pressure, bonding duration and specific glue consumption. Regression models describing the dependence of bending strength and modulus of elasticity in bending on the investigated technological bonding parameters are estimated. The obtained experimental and model-based results are analysed and discussed.*
Keywords*: CONSTRUCTION, WOOD, PLYWOOD, BENDING STRENGTH, MODULUS OF ELASTICITY IN BENDING, MATHEMATICAL MODELING, BLACK LOCUST (ROBINIA PSEUDOACACIA).*

1. Introduction

Wood is one of the most popular and widely used building materials, with the construction sector being the largest consumer of wood and timber. Its use as a building material is exclusively due to the large number of the positive properties of wood materials [1-4]: relatively low bulk density, easy machinability, significant compressive and tensile strength, low thermal conductivity and others. Last but not least are the positive environmental aspects and the possibility for recovery and renewal of wood resources.

At the same time, the plant origin of wood determines many disadvantages - anisotropic structure, hygroscopicity and the associated variability of shape and size, resistance to various biological attacks and the ability to burn. The modern woodworking industry has accumulated centuries of experience in solving the problems of wood deficiencies. On the one hand, technologies have been developed to protect and modify wood in order to increase its durability and reduce its hygroscopicity and flammability, as well as to increase some of its strength characteristics. The other increasingly fast-growing direction, which eliminates the shortcomings of wood and adds new properties, is the development of wood composite materials, which are increasingly used in construction.

Such wood composite material is plywood, which is most widely used in construction. The main tree species on which plywood production in Bulgaria is based in recent years are poplar and beech. The stocks of raw materials of these types, suitable for plywood production, are constantly decreasing, and at the current rate of exploitation of the forests, the stocks of beech will disappear in the next 2-3 decades, and the stocks of poplar are already running out. This makes it necessary to look for opportunities for the production of plywood from other wood species, from which there are stocks of wood. Such a tree species for our country is the black locust (*Robinia pseudoacacia*), from which there are significant stocks of wood, which so far do not find wide economic application.

The main goal of the present work is to determine the modulus of elasticity in bending and bending strength and to investigate the influence of the main technological bonding factors on these two indicators for a new type of plywood for construction, made of black locust wood.

2. Experimental results and analysis

The materials needed for the research were black locust veneer with a nominal thickness of 2.2 mm and water-soluble phenol-formaldehyde adhesive. These materials were used for the production in laboratory conditions of six-layer, black locust, waterproof plywood for construction with a nominal thickness of 12 mm.

The current investigation aims to establish the influence of the main technological factors in bonding on the modulus of elasticity in bending and bending strength.

The first factor (z_1) is the temperature of the press platens. The range of its variation was determined according to the manufacturer's recommendations in the interval from 120˚C to 160˚C.

The second factor (z_2) is the specific pressure. The interval of its variation was determined by recommendations in the specialized literature. The levels of variation are 1 MPa, 1.5 MPa and 2 MPa.

The third factor (z_3) is the duration of plywood pressing. The range of its variation was determined according to the recommendations of the adhesive manufacturer and from the recommendations for the duration of plywood pressing given in the specialized literature. The levels of variation are as follows: 8 min; 11 min and 14 min.

For fourth factor (z_4) is the specific glue consumption (specific cost). The range of its variation was determined according to the recommendations of the adhesive manufacturer and from the recommendations for specific glue consumption given in the specialized literature. The experimental region for the specific glue consumption is from 100 g/m^2 to 200 g/m^2.

The chosen experimental design was optimal composite design [5] with four control factors: temperature of press plates, pressure, specific glue consumption and duration of pressing. The number of experimental runs in the experimental design is 24. Additional (repeated) three experiments have been made at the central point of the design, where all factors are set equal to the values in the middle of their variation region. Six measurements the mechanical properties of obtained black locust plywood plates the modulus of elasticity in bending (y_1) and bending strength (y_2) are performed for each experimental run and the results are averaged. Thus, the total number of conducted measurement tests is 162.

Table 1. *Data from repeated observations.*

	Elasticity in bending y_1	Bending strength y_2
Mean value	14218.70 N/mm^2	124.86 N/mm^2
St. deviation	458.39 N/mm^2	8.27 N/mm^2

The results for the means and the standard deviations from the repeated experimental runs in the at the central point of the design at constant levels of the process parameters: the temperature of the press platens z_1 = 140 ˚C, specific pressure z_2 = 1.5 MPa, duration of plywood pressing z_3 = 11 min and specific glue consumption z_4 = 150 g/m^2 are presented in Table 1.

The determination of the modulus of elasticity in bending and bending strength was performed according to the standard BDS EN 310: 1999 Wood based panels: Determination of the modulus of

elasticity in bending and bending strength [6]. This European Standard describes the method for determining the modulus of elasticity in bending and bending strength of wood - based panels with a nominal thickness equal to or greater than 3 mm.

3. Model-based investigation results

Regression models are estimated the modulus of elasticity in bending (y_1) and bending strength (y_2) of the produced black locust plywood plates as a function of the temperature of the press platens (x_1), the specific pressure (x_2), the duration of plywood pressing (x_3) and the specific glue consumption (x_4) in coded in the region [-1 ÷ 1] units [7]. The relation between coded (x_i) and natural (z_i) units can be expressed by the equation:

$$x_i = (2z_i - z_{i,max} - z_{i,min})/(z_{i,max} - z_{i,min}). \quad (1)$$

where $z_{i,max}$ and $z_{i,min}$ are the maximal and the minimal values, determined by the experimental regions of each of the investigated process parameters. The regression models, together with the determination coefficients are presented in Table 2.

Table 2. *Regression models.*

	Regression models	***R^2, %***
y_1	$y_1 = 12002.53 - 1052.90x_1 - 193.13x_2 + 774.01x_4 - 1577.36x_1^2 + 903.95x_3^2 + 1111.56x_4^2 - 297.49x_1x_2 + 211.18x_3x_4 + 259.65x_1x_4 + 1273.47x_1x_2^2 - 256.87x_1x_2x_4 - 569.71x_1^2x_4$	90.92
y_2	$y_2 = 138.70 - 12.06x_1 + 4.40x_4 + 6.88x_1^2 - 18.38x_4^2 - 4.55x_1^2x_2 + 3.11x_2x_3 + 2.88x_2x_4 + 13.28x_1x_2^2 - 3.61x_1x_2x_3 + 4.72x_1x_2x_4 + 2.20x_2x_3x_4$	85.94

The goodness of fit tests and the values of the determination coefficients show good prediction characteristics of the estimated models. They can be used for the choice of appropriate process parameters under given technological requirements for the modulus of the elasticity in bending (y_1) and the bending strength (y_2) during the production of black locust plywood.

The estimated regression models are used for the investigation of the dependencies of the modulus of the elasticity in bending (y_1) and the bending strength (y_2) of the produced black locust plywood plates as on the variation of the process parameters: the temperature of the press platens (z_1), the specific pressure (z_2), the duration of plywood pressing (z_3) and the specific glue consumption (z_4), visualized on the contour plots in Fig. 1 – Fig. 4.

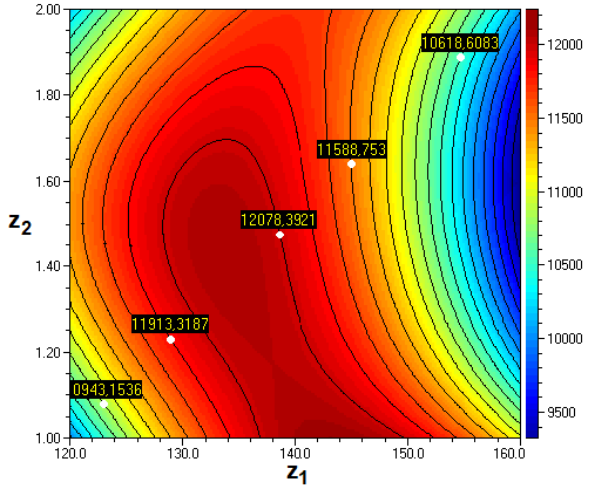


Fig. 1 *Contour plot of the bending elasticity (y_1) vs. the temperature of the press platens (z_1,˚C) and the specific pressure (z_2, MPa) for z_3 = 11 min and z_4 = 150 g/m^2.*

In Fig. 1 the contour plot of the elasticity in bending (y_1) as a function of the temperature of the press platens (z_1,˚C) and the specific pressure (z_2, MPa), for constant values of the duration of plywood pressing (z_3) and the specific glue consumption (z_4): z_3 = 11 min and z_4 = 150 g/m^2. It can be seen that under the specified conditions, the factor with larger influence is the temperature of the press platens (z_1). The region, where the maximal values of the elasticity in bending (y_1) can be obtained for temperatures of the press platens (z_1) in the region from 132˚C to 146˚C and specific pressure values below 1.6 MPa.

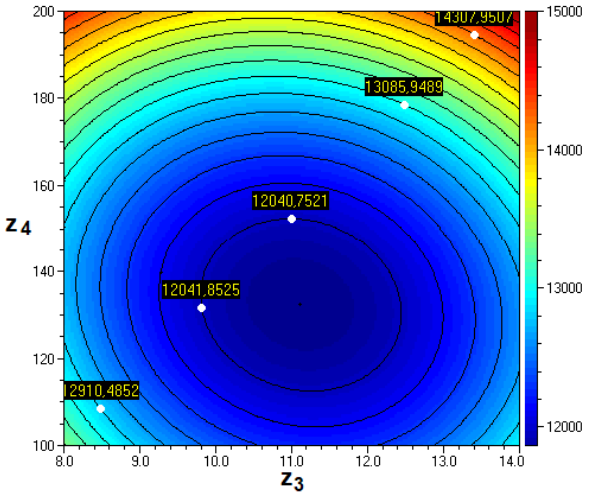


Fig. 2 *Contour plot of the bending elasticity (y_1) vs. the duration of plywood pressing (z_3, min) and the specific glue consumption (z_4, g/m^2), for z_1 = 140 ˚C and z_2 = 1.5 MPa.*

Fig. 2 presents the contour plot of the bending elasticity (y_1) as a function of the duration of plywood pressing (z_3, min) and the specific glue consumption (z_4, g/m^2), for constant values of the temperature of the press platens and the specific pressure, z_1 = 140 ˚C and z_2 = 1.5 MPa. It can be seen that the highest values of the bending elasticity are obtained for the highest values of the specific glue consumption z_4 > 190 g/m^2 for the set by factors z_1 and z_2 conditions.

The contour plot of the dependence of the bending strength (y_2) on the temperature of the press platens (z_1,˚C) and the specific pressure (z_2, MPa) for constant values of the duration of plywood pressing (z_3) and the specific glue consumption (z_4): z_3 = 11 min and z_4 = 150 g/m^2 is presented in Fig. 3. The maximal values of the bending strength in this case are obtained for lowest values of the temperature of the press platens around 120˚C and specific pressure in the region 1.3 ÷ 1.5 MPa.

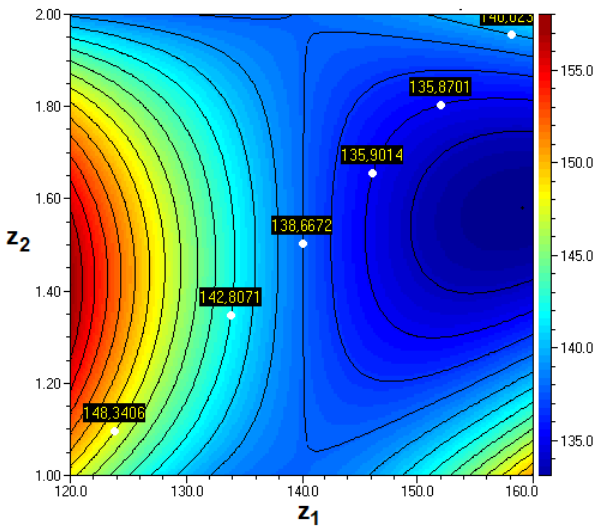


Fig. 3 *Contour plot of the bending strength (y_2) vs. the temperature of the press platens (z_1,˚C) and the specific pressure (z_2, MPa) for z_3 = 11 min and z_4 = 150 g/m^2.*

In Fig. 4 is presented the contour plot of the bending strength (y_2) vs. the duration of plywood pressing (z_3, min) and the specific glue consumption (z_4, g/m^2), for constant values of the temperature of the press platens and the specific pressure, z_1 = 140 ˚C and z_2 =

1.5 MPa. It can be seen, that under the set conditions, the bending strength (y_2) is not dependent on the duration of plywood pressing (z_3, min), while the choice of the specific glue consumption (z_4, g/m^2) is important and for obtaining the maximal values of the bending strength, the specific glue consumption should be set in the region 150 ÷ 160 g/m^2.

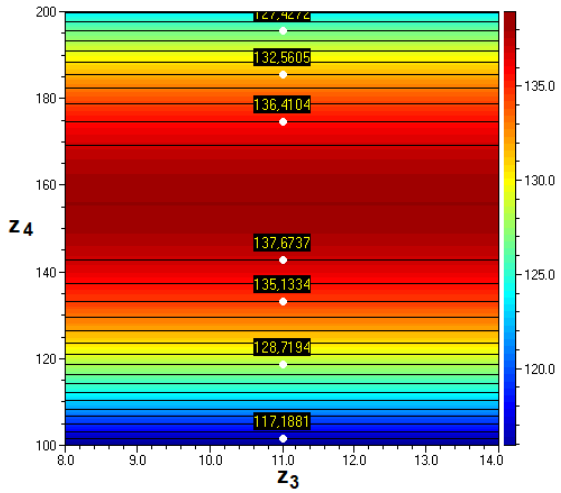


Fig. 4 *Contour plot of the bending strength (y_2) vs. the duration of plywood pressing (z_3, min) and the specific glue consumption (z_4, g/m^2), for z_1 = 140 °C and z_2 = 1.5 MPa.*

From the obtained investigation results is seen that the changes of all factors influence the values of the investigated mechanical properties - the modulus of elasticity in bending (y_1) and bending strength (y_2) of the produced black locust plywood plates. The choice of optimal regimes should be performed at defining concrete technological requirements for all quality characteristics simultaneously.

Experimental studies on the modulus of elasticity in bending and bending strength for construction black locust plywood bonded with phenol-formaldehyde adhesive confirm the patterns and trends of previous studies on the same properties but for black locust plywood [bonded with urea-formaldehyde]. Both indicators depend very much on the wood species from which the plywood is made, and in both studies the respective black locust plywood is superior in values to the respective beech and poplar plywood. This is due to the higher mechanical properties of black locust wood, compared to the same for beech and poplar. Technological factors in gluing also have a decisive influence on the values of the two indicators, as the temperature of the press platens and the specific glue consumption are formed as slightly more important for the final results.

4. Conclusions

The current investigation aims to establish the influence of the main technological factors in bonding on the modulus of elasticity in bending and bending strength.

For the experimental investigation an optimal composite design is realized with four control factors: temperature of press plates, pressure, specific glue consumption and duration of pressing. The number of experimental runs in the experimental design is 24 and 3 additional experiments have been made at the central point of the design. Six measurements the mechanical properties of obtained black locust plywood plates the modulus of elasticity in bending (y_1) and bending strength (y_2) are performed for each experimental run. Thus, the total number of conducted measurement tests is 162.

Regression models for the modulus of elasticity in bending (y_1) and bending strength (y_2) of the produced black locust plywood plates are estimated as a function of the temperature of the press platens (x_1), the specific pressure (x_2), the duration of plywood pressing (x_3) and the specific glue consumption (x_4). The obtained dependencies of the two quality characteristics on the process parameters are used for investigation and prognostication.

Research confirms the good prospects for the introduction of this new type of plywood in construction.

Acknowledgements

The authors want to thank for financial support from the National Science Program "Information and Communication Technologies for a Digital Single Market in Science, Education and Security (ICTinSES)", funded by the Bulgarian Ministry of Education and Science.

References

1. G. Blaskova, Properties and use of black locust wood. *Furniture and woodworking industry* (Sofia) 3 (2000)
2. G. Blaskova, *Wood Science* (Publishing house at LTU, Sofia, 2003)
3. P. Panayotov and team, Report on the topic: "Comparative studies of the properties of the wood of the straight black locust Robinia pseudoacacia forma rectissima and the traditionally used white acacia Robinia pseudoacacia L.". MES, FSI at LTU-Sofia, PSIL for wood modification, Sofia, (2004)
4. A. Hristov, Sci. researches of the Union of Scientists in Bulgaria - Plovdiv. Series C. Tech. and Technol., **V**, Balkan Conf. of Young Scient. (Plovdiv) 39-46 (2005)
5. I. Vuchkov, *Experimental research and identification* (Technique, Sofia, 1990)
6. BDS EN 310: 1999 "*Wood-based panels. Determination of the modulus of elasticity in bending and bending strength*".
7. *QstatLab home page*: http://www.qstatlab.co.uk/eng/index.html

Modelling uncertainty in multisensory systems at conflict measurements with dempster-shafer combinatorial rule

Varbanov Vladimir
Institute of Metal Science, Equipment and Technology with Hydroaerodynamic Center at Bulgarian Academy of Sciences, 67 Shipchenski Prohod Street, 1574 Sofia, Bulgaria
vdvarbanov@abv.bg

Abstract: *Decision making in conflict data is a problem that plague the information fusion. It is usually resolved by the use of probabilistic methods such as Bayes. Still Bayes becomes impractical in strong presence of conflicts or lack of data. In that case Dempster–Shafer (DS) evidence theory is applied, because of its ability to handle conflicting sensor inputs. Because of that, DS-based information fusion is very popular in decision-making applications, although the classic combinatorial rule may produce counter intuitive results, especially when combining evidences with high level of conflict. The paper present a method which can be applied to the decision making process, thus resolving this problem.*

Keywords*: Dempster-Shafer, Dempster-Shafer evidence distance*

1. Introduction

Information fusion technology is usually used to analyze multisource uncertain information. A multi sensor system has significant advantages over single sensor systems, especially when combined proper algorithm :

- Robustness – the the system provides overlapping information, regarding the observed event, thus mitigating contribution of fault sensor to the accuracy of decisions and measurement.
- Multi dimensionality of measurements – a multisensory system can receive information from sources in different domain which enrich the quality of the data and decrease the chance of interference.

The problem is that this advantages in multisensory systems can easily be turned in to liabilities. For small number of sensors a fault sensor can make the decision process impossible, mainly because the system will be unable to single out the defected device or sensors in case of sensor working in different physical domain a high level of conflict may occur even though each one of the sensors is working properly. In example measuring distance with laser and sound may lead to conflict in case of transparent obstacle although both sensors are working as intended. In order to obtain reliable information from fusing measurements in cases of conflict a suitable mathematical methods are needed and Dempster-Shafer theory of evidence can be applied in such cases. Proposed at first in 1967 by Demster and the developed into its current form in 1976 by Shafer the method suffered from the very same issues mentioned above. Counter intuitive results were generated if the input data was conflicted. However nowadays this method is preferred for such cases. To solve such a problem, two major methodologies are popular. One is to preprocess the bodies of evidence (BOEs) and the other is to modify the combined rule. There are many modifications to the combinatorial rule Dubois and Prade's disjunctive Yager's combination rule and others. All of the most used rules has their pros and cons and careful consideration of athe advantages and disadvantages of each of them is needed in ordro to be achieved stable logic. The methodology of preprocessing bodies of evidences is based on distance from evidence. There are different methods proposed by Sang, Yong and Anne-Laure Jousselme.

2. Dempster–Shafer Combinatorial rule

2.1 Frame of discern (FOD)

The frame of discernment contains M mutually exclusive and exhaustive events.

$$\Theta = \{\theta_1, \theta_2, \theta_3 \cdots \theta_M\} \quad (1)$$

The representation of uncertainties in the DS theory is similar to that in conventional probability space Θ, although DS probabilities are defined as masses and are view more as options instead of physical world probabilities. The DS theory also allows this "probabilities" to be assigned to subsets of Θ - $\{\theta_i, \theta_j, \cdots \theta_n\}$ as well to individual element θ_i. Accordingly, we can derive a power set of DS theory which includes all the combinations of the events of Θ and consists of 2^M elements:

$$2^\Theta = \{\emptyset, \{\theta_1\}, \{\theta_2\}, \ldots, \{\theta_1, \theta_2\}, \ldots \Theta\} \quad (2)$$

where ∅ is the empty set.

2.2. Basic Probability Assignment (BPA)

Mass function (mass) is a function, $m: 2^\Theta \rightarrow [0,1]$ that satisfies the following equations:

$$m(\emptyset) = 0 \quad (3)$$

$$\sum m(\theta) \forall \theta \in 2^\Theta = 1 \quad (4)$$

Equation (3) means that the empty does not take part in forming decision according to DS combinatorial rule, while equation means that cumulative mass is normalized. Elements of power set having $m(\theta) > 0$ are called focal elements.

2.3. Dempster–Shafer Rule of Combination

The data fusion summarizes the information, obtained from multiple independent sources and as such DS combination rule emphasizes the agreement between multiple sources and ignores all the conflicting evidences through normalization. Any two mass functions B and C over the same FOD with at least one focal element in common can be combined into a new mass function[1,2]. The weight of the mass stands for the strength of our belief in the proposition that is represented to us. In other word the combination perform orthogonal sum ⊕ on the input evidences. The combination rule for two evidences m_1 and m_2 is written with the following expression :

$$m_{1,2}(A) = \sum B \cap C = \frac{\{\{m_1(B)\}.\{m_2(C)\}\}}{1-K} \quad (5)$$

when $A \neq \emptyset$ and $m(\emptyset) = 0$.
Where K is the degree of conflict in the two evidences:

$$K = \sum B \cap C = \{m_1(B) m_2(C)\} \quad (6)$$

when $B \cap C = \emptyset$

2.4. Belief and Plausibility Function
Belief function for element A, otput of which is defined as:

$$Bel(A) = \sum_{B \subset A} m(B) \quad (7)$$

Where focal element A can be set, i.e. $A = \{\theta_1, \theta_2\}$ or singleton $A = \{\theta_1\}$ and represents a statement/opinion and $Bel(A)$ measures the belief that the this statement A is fully supported by B. $m(A)$ measures the amount of belief that one commits exactly to A alone(not supported by other evidences).

Plausibility is define as

$Pl(A) = \sum_{B \cap A} m(B)$ (7)

Plausibility measures the hesitation of correctness of statement A, because A is just partially supported by B. Of $Pl(A)$ can be taught as the total belief mass that might be moved into A, whereas Bel(A) measures the total belief mass that is constrained to A.

Example 1.

Given $m(A) = 0.51$, $m(B) = 0.23$, $m(C) = 0.06$ and $m(A, B, C) = 0.20$

$Bel(A, B) = m(A) + m(B) = 0.51 + 0.23 = 74$ (8)

$Pl(A, B) = m(A) + m(B) + m(A, C) + m(B, C) + m(A, B) + m(A, B, C) = 0.94$ (9)

3. Paradoxes in DS combination rule

3.1 Veto paradox

For multi sensorial datafusion according to Dempster-Shafer rule if one sensor of the sensors has completely contradict the others it invalidates the evidences of all the other, no matter that they show similar data.

Example 2. Let have four sensors and four evidences in the frame of discern $\Theta = \{A, B, C\}$ and every one of them) f rom Fig.1 every object can be put in one of

Sensor 1: $m_1(A) = 0.6, m_1(B) = 0.2, m_1(C) = 0.2$

Sensor 2: $m_2(A) = 0.0, m_2(B) = 0.9, m_2(C) = 0.1$

Sensor 3: $m_3(A) = 0.7., m_3(B) = 0.15, m_3(C) = 0.15$

Sensor 4: $m_4(A) = 0.7., m_4(B) = 0.15, m_4(C) = 0.15$

It can be seen that sensor 2 is faulty, as its mass for A is equal to two. Applying equation (5) will produce output $m_{1,2}(A) = 0$, next when we apply same equation and fuse the result with the third sensor we will obtain same result for $m_{1,2,3}(A) = 0$ and again will have same result for $m_{1,2,3,4}(A) = 0$. One defected sensor which is clearly an outlier can compromise the whole fusion process[5,4].

3.2 Total trust paradox

This paradox occurs if two or more sensors have strong, conflicting evidences, and weak overlapping evidences.

Example 3.

$\Theta = \{A, B, C\}$

Sensor 1: $m_1(A) = 0.95, m_1(B) = 0.05, m_1(C) = 0$

Sensor 2: $m_2(A) = 0, m_2(B) = 0.1, m_2(C) = 0.9$

Applying DS combination rule(equation (5)), we get $m_{1,2}(A) = 0$, $m_{1,2}(B) = 1$, and $m_{1,2}(C) = 0, K = 99$. Here, both masses for evidences A and B are nullified and because of normalization $m_{1,2}(B) = 1$, which is counterintuitive.

4. Elimination of the paradoxes

Widely used in DS theory in strong cases of conflict is the Yager rule. There the mass associated with conflict is directly added to the subset consisting all singletons, which can be interpreted as ignorance, he also omits normalization and allow the ground probability mass assignment of the null set to be greater than $m(\emptyset) \geq 0$, thus adding spreading the values of the fusion into more non zero elements. This work around fixes the nullifying effect in the veto and total trust paradox[6].

5. Conclusion

Dempster-Shafer is often viewed as generalized Bayes. Biggest advantages of which is the pore realx definition of the term probability which allows to formalize decision making process similar to the probabilistic without knowing the conditional probabilities. The method is prone to high conflicting input data but so is Bayes. However these shortcomings are fixed be use of modified combinatorial rules. This is why the Dempster-Shafer theorem is widely used in Neural network, machine learning, autonomous driving cars as well as computer vision[3,4].

The results are aimed at the implementation of Work Package 2 "Intelligent Security Systems" of project BG05M2OP001-1.002-0006 "Construction and development of the Competence Center "Quantum Communication, Intelligent Security Systems and Risk Management (Quasar)", which has received funding from the European Regional Development Fund through the Operational Program "Science and Education for Smart Growth" 2014-2020.

5 References

1. Shafer, G. A Mathematical Theory of Evidence. Princeton University Press: Princeton. NJ. USA, 1976. Volume 42.

2. Fourati, H. Multisensor Data Fusion: From Algorithms and Architectural Design to Applications. CRC Press: Boca Raton. FL. USA . 2015.

3 N. Dalal and B. Triggs. Histograms of oriented gradients for human detection. in Computer Vision and Pattern Recognition, 2005. CVPR 2005. IEEE Computer Society Conference on, vol.1.IEEE, 2005, pp. 886–893.

4.Coombs, K. Freel. D.; Lampert. D.; Brahm. S.J. Sensor Fusion: Architectures. Algorithms. and ApplicationsIII. Int. Soc. Opt. Photonics **1999**. 3719. 103–113.no. 15. pp. 2895–2907, 2003.

5. Dempster, A.P. Upper and Lower Probabilities Induced by a Multivalued Mapping, in Classic Works of the Dempster-Shafer Theory of Belief Functions; Springer: Berlin/Heidelberg, Germany, 2008; pp. 57–72.6. Yager, R.R. On the Dempster-Shafer framework and new combination rules. Inf. Sci. **1987**, 41, 93–137.

6.Yager, R.R. On the Dempster-Shafer framework and new combination rules. Inf. Sci. **1987**, 41, 93–137.

Adiabatical thermodynamic manner of the description of the carbon dioxide pollutant excess of Earth's atmosphere

Mihai Petrov
University "Pr. Assen Zlatarov", Burgas
Faculty of Real Sciences, Department of Physics and Mathematics
galantusgratus@abv.bg

Abstract: *The problem of study of the atmospheric state with the accumulation of polluting gases in the atmosphere as a result of anthropogenic activity is very actually. One of the major polluting gases at large ratios is carbon dioxide. The recent study aims to obtain a quantitative expression of the variation of the atmospheric temperature as the result of the variations of carbon dioxide concentrations. It is known that the state of the atmospheric gas is described approximately by the model of the ideal gas. As the altitude increases, the gas pressure and the temperature in the troposphere decrease. The adiabatic constant of atmospheric air can be found from the adiabatic equation which is based on the ideal gas model. The natural logarithm of the pressure depending on the natural logarithm of the temperature allows the determination of this adiabatic constant. The obtained result coincides within the limits of the real ones, fact that denotes the correctness of the application of the ideal gas model. The known data of the pressure as a function of height allow to determine the fictive molar mass of the atmospheric gas from the dependence of the natural logarithm of pressure as a function of the altitudes and the result of the fictive molar mass coincides within the limits of the real ones. NASA observatories periodically record from the 1980s until now the permanent increase of the average temperature of the atmosphere with a speed of the order of (0,02 ^oC/year) and of the concomitant increasing of the concentration of carbon dioxide in the atmosphere. This fact currently concludes that the increase of global average temperature is influenced by the increase of the concentration of carbon dioxide. These concomitant increases allow to elaborate one empirical expression of the variation of the global average temperature depending on the variation of the carbon dioxide concentration. The obtaining of this empirical expression is based on the equation of state of the ideal gas and also on the adiabatic equation. The graphical representation of the temperature variation as a function of the concentration variation allows the recalculation of the adiabatic constant of the atmospheric air which value is within the limits of the real ones and denotes the validity and correctness of the suggested method. The recalculated values of the temperature variation according to the empirical formula must coincide with the real ones recorded. The coincidence is confirmed by the functional dependence $\Delta Te = f(\Delta T)$. In order to ascertain the average speed of accumulation of carbon dioxide in the atmosphere, the graph of the dependence $\Delta C = f$ (time) is represented which proportionality coefficient is the accumulation speed of order (3,833 mg / m^3/ year).*

***Keywords**: ADIABATIC MODEL, ADIABATIC CONSTANT, MOLAR CONCENTRATION, BAROMETRIC FORMULA, EMPIRICAL EXPRESSION*

1. Introduction

The current state of the atmosphere is described by the presence of pollutants in both gas and aerosols that have a negative effect on the evolution of the biosphere and on the state of the atmosphere. Modern anthropogenic activity is characterized by the increasing of the concentrations of gaseous pollutants that have a green house effect. One of the major green house components is carbon dioxide which has a ratio of 75% in comparison to other pollutants and therefore the effect is based only on carbon dioxide and the other components are of minor importance and almost have no influence. The empirical method suggested in this study is based on deeply analysis that applies in general the model of ideal gas.

The application of the model of ideal gas for atmospheric air allows to check the calculated values with the real ones such as the effective molar mass of the air and the adiabatic constant. The validity of the suggested method is confirmed by re-calculation of the important parameters such as the molar mass and the adiabatic constant and which are coincident with the real ones. The practical importance of this expression is based on the fact that the anthropogenic accumulation of carbon dioxide is followed by the accumulation of heat excess in the atmosphere, and in its turn the increasing of the average global temperature of the atmosphere. One thing it is important to mention that the effect which always takes place must be explained and this explanation is given by physical methods based on thermodynamic phenomena for the atmosphere.

2. The adiabatic model of atmosphere with the excess of carbon dioxide

The composition of the dry air is complex and it contains 78,08 % nitrogen, 20,95% oxygen, 0,93% argon, 0,04% carbon dioxide and small amounts of other gases. [1] The temperature of the troposphere is highest near the surface of the Earth and decreases with the altitude. The average temperature gradient of the troposphere is 6.5°C per 1000 m of altitude. An important parameter that describes the dependence of the temperature as the function of height is the rate $-\frac{dT}{dh}$, (h is the altitude). This rate is called the environmental lapse rate.[2],[3],[4] The ELR assumes that the air is perfectly still, i.e. that there is no mixing of the layers of air from vertical convection and no winds that would create turbulences. The dry adiabatic lapse rate accounts for the effect of the expansion of dry air as it rises in the atmosphere and wet adiabatic lapse rates include the effect of the condensation of water steam on the lapse rate. Since the process of compression and expansion of an air parcel can be considered reversible and no energy is transferred into or out of the parcel, such a process is considered isentropic, meaning that there is no change in entropy as the air parcel rises and falls ($dS=0$).Since the heat exchanged ($dQ=0$) is related to the entropy change dS by $dQ=TdS$, then:

$$\frac{dS}{dh} = 0 \tag{1}$$

where S is the entropy. The above equation states that the entropy does not change with height. The rate at which temperature decreases with height under such conditions is called the adiabatic lapse rate.[5] For dry air is valid the adiabatic equation of the ideal gas [6]:

$$P(h) \cdot \left[T(h)\right]^{-\frac{\gamma}{\gamma-1}} = const \tag{2}$$

where γ is the adiabatic constant of the air (γ ≈ 7/5). Combining with the equation for the pressure, then the expression of dry adiabatic lapse rate [7]:

$$\frac{dT}{dh} = -\frac{M \cdot g}{R} \cdot \frac{\gamma - 1}{\gamma} = -9{,}8^0 C / km \tag{3}$$

The pressure of the atmosphere is maximum at sea level and decreases with altitude [8]. This is because the atmosphere is very nearly in hydrostatic equilibrium so that the pressure is equal to the weight of air above a given point. The change in pressure with altitude can be expressed by the density as[9]:

$$\frac{dP}{dh} = -\rho \cdot g = -\frac{M \cdot P \cdot g}{R \cdot T} \quad (4)$$

where g is the gravitational acceleration; ρ is the density of air; h is the altitude; P is the pressure; R is the gas constant; T is the thermodynamic temperature; M is the molar mass.

This change in pressure (4) originates from the barometric formula of troposphere [10]:

$$P(h) = P_o \cdot e^{-\frac{M \cdot g \cdot h}{R.T(h)}} \quad (5)$$

Combining the expressions of adiabatic process (2) with (5), then:

$$P_o \cdot e^{-\frac{M \cdot g \cdot h}{R.T}} \cdot [T(h)]^{-\frac{\gamma}{\gamma-1}} = const \quad (6)$$

If the temperature depends on height, it would be better to obtain by the application of (6) such expression of the value of temperature that depends on height:

$$[T(h)]^{-\frac{\gamma}{\gamma-1}} = \frac{const}{P_o} \cdot e^{\frac{Mgh}{RT(h)}} \quad (7)$$

$$[T(h)]^{\frac{\gamma}{\gamma-1}} = \frac{P_o}{const \cdot e^{\frac{Mgh}{RT(h)}}} \quad (8)$$

The procedure of natural logarithm of (8) gives:

$$\frac{\gamma}{\gamma-1} \cdot \ln[T(h)] = \ln P_o - \ln(const) - \frac{Mgh}{RT(h)} \quad (9)$$

$$T(h) \cdot \ln[T(h)] = \frac{T(h) \cdot (\gamma-1)}{\gamma} \cdot (\ln P_o - \ln(const)) - \frac{Mg \cdot (\gamma-1)h}{R \cdot \gamma} \quad (10)$$

$$\ln[T(h)] = \frac{(\gamma-1)}{\gamma} \cdot (\ln P_o - \ln(const)) - \frac{Mg \cdot (\gamma-1) \cdot h}{R \cdot \gamma \cdot T(h)} \quad (11)$$

The graphic of the dependence $\ln[T(h)] = f\left(\frac{h}{T}\right)$ is represented on the Fig.1 For the case when $h=0$, then $h/T=0$ and the expression (11) is:

$$\ln[T(0)] = \frac{(\gamma-1)}{\gamma} \cdot (\ln P_o - \ln(const)) \quad (12)$$

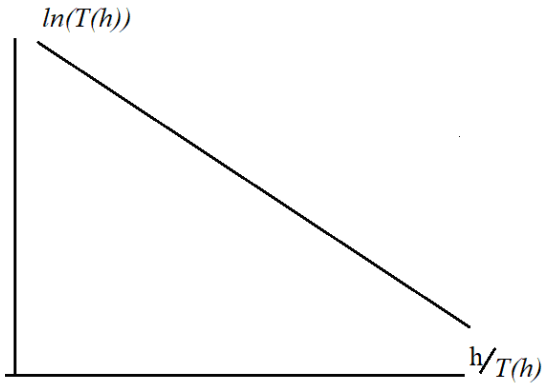


Fig.1 *The dependence of* $\ln[T(h)] = f\left(\frac{h}{T}\right)$

Such a way, it would be possible to recalculate the temperature at the null level T(0) and also the molar mass M by the slope of this graphic. The expression (12) could be applied for the small altitudes. Then:

$$\ln T = \frac{(\gamma-1)}{\gamma} \cdot (\ln P - \ln(const)) \quad (13)$$

In order to describe the increasing of the temperature due to of the greenhouse effect, it would be better to differentiate the expression (13):

$$\frac{\Delta T}{T} = \left(\frac{\gamma-1}{\gamma}\right) \cdot \frac{\Delta P}{P} \quad (14)$$

The respective expression of the equation of the state of ideal gas: $P.V = \nu.R.T$; $P = C.R.T$; C is the molar concentration of the mixture of gas of the atmospheric air. The respective variation of pressure:

$$\Delta P = R \cdot (\Delta T.C + \Delta C.T) \quad (15)$$

The substitution of (15) into (14) gives:

$$\frac{\Delta T}{T} = \left(\frac{\gamma-1}{\gamma}\right) \cdot \frac{(C.\Delta T + T.\Delta C)}{C.R.T} =$$

$$= \left(\frac{\gamma-1}{\gamma}\right) \cdot \left(\frac{\Delta T}{R.T} + \frac{\Delta C}{C.R}\right) = \left(\frac{\gamma-1}{\gamma}\right) \cdot \frac{\Delta T}{R.T} + \left(\frac{\gamma-1}{\gamma}\right) \cdot \frac{\Delta C}{C.R}$$

$$\Delta T = \left(\frac{\gamma-1}{\gamma(R-1)+1}\right) \cdot \frac{\Delta C \cdot T}{C} \quad (16)$$

The expression (15) shows quantitatively the increasing of the temperature of the atmosphere with the increasing of the molar concentration of greenhouse gases by the value ΔC.

The density of air at sea level is about 1,2 kg/m^3. The atmospheric density decreases as the altitude increases. [11]

Then the molar concentration of the atmospheric air is calculated as:

$$C = \frac{\rho}{M} = \frac{1{,}2(kg/m^3)}{0{,}029(kg/mol)} = 41{,}37(mol/m^3) = 0{,}04137(mol/l)$$

The average mass of the atmosphere is about 5 quadrillion ($5{,}13 \times 10^{15}$) tones or 1/1,200,000 the mass of Earth [10]. The mass of the atmosphere that is $5{,}13.10^{18}$ kg allows to calculate the full volume of the atmosphere - $V_{atm.}$:

$$V_{atm} = \frac{m_{atm}}{M \cdot C} = \frac{5{,}13.10^{18}(kg)}{0{,}029(kg/mol) \cdot 0{,}04137(mol/l)} =$$

$$= 4275{,}96.10^{18}(l) = 4275{,}96.10^{15}(m^3) = 4{,}28.10^{18}(m^3)$$

Then, easily we can calculate the height of troposphere - h:

$$h = \frac{V_{atm}}{S_{Earth}} = \frac{4{,}28.10^{18}}{4.3{,}14.(6371.10^3)^2} =$$

$$8{,}39.10^{-9}.10^{18}.10^{-6} = 8{,}39.10^3(m) \cong 8{,}5(km)$$

The calculated value of molar concentration of air will be used to appreciate the change of the temperature as the result of increasing of greenhouse gases by the value ΔC. In general the average temperature of the atmospheric air is increasing almost linearly the last 50 years. [12] (Fig. 2)

The opinions about the reason of the increasing of the temperatures are various, but the most observation is on the focusing of the increasing of the concentration of carbon dioxide that is one major greenhouse gas and the carbon dioxide has 75% effect from all others green house gases [14]. The registration of the concentrations of carbon dioxide by the satellites [14] is represented by the diagram in the Fig. 3.

The changes of the values of temperatures and concentrations which are described by the figures 2 and 3 could be included into the expression (15) and the final result is the representation of the graphic $\Delta T = f(\Delta C)$ that in general is a linear dependence (Fig. 4)

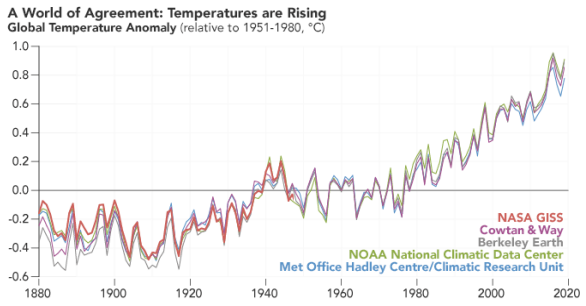


Fig. 2. *The history of global change of the temperature [13]*

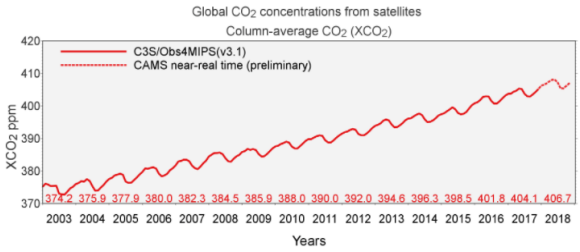


Fig. 3 *The dynamics of the change of the concentration of CO_2 [14]*

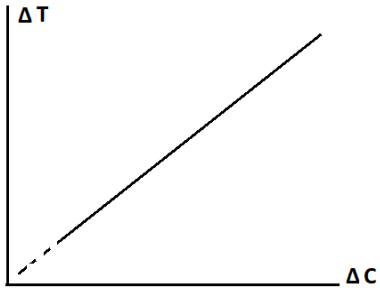


Fig. 4 *The form of the dependence of $\Delta T=f(\Delta C)$*

Such a way, the slope of the dependence of $\Delta T=f(\Delta C)$ allows to re-calculate the value of adiabatic constant γ. The numerical value of γ confirms the validity of the suggested quantitative expression of the temperature variation.

Results and discussion

The values of temperatures and of the pressure are changeable with the altitude. The following Table 1 shows the results [11] of the measurements of these values.

Table 1. *The important parameters of the atmosphere as the function of altitude [11]*

Geo potential Altitude above Sea Level - h - (m)	Temperature - t - (°C)	Acceleration of Gravity - g - (m/s^2)	Absolute Pressure - p - (10^4 N/m^2)	Density - ρ - (kg/m^3)	Dynamic Viscosity - μ - (10^{-5} $N\,s/m^2$)
-1000	21.50	9.810	11.39	1.347	1.821
0	15.00	9.807	10.13	1.225	1.789
1000	8.50	9.804	8.988	1.112	1.758
2000	2.00	9.801	7.950	1.007	1.726
3000	-4.49	9.797	7.012	0.9093	1.694
4000	-10.98	9.794	6.166	0.8194	1.661
5000	-17.47	9.791	5.405	0.7364	1.628
6000	-23.96	9.788	4.722	0.6601	1.595
7000	-30.45	9.785	4.111	0.5900	1.561
8000	-36.94	9.782	3.565	0.5258	1.527
9000	-43.42	9.779	3.080	0.4671	1.493
10000	-49.90	9.776	2.650	0.4135	1.458

In order to validate the expression (2) by the application of real values of the source [11], the following graphic $\ln[P(h)] = f(\ln[T(h)]$ is represented on Fig. 5. The procedure of natural logarithm of the expression (2) is:

$$\ln\left[P(h)\cdot[T(h)]^{\frac{\gamma}{\gamma-1}}\right] = \ln[const];$$

$$\ln[P(h)] = \frac{\gamma}{\gamma-1}\cdot\ln[T(h)] + \ln[const]$$

The slope of this linear dependence allows to find the adiabatic constant γ of air.

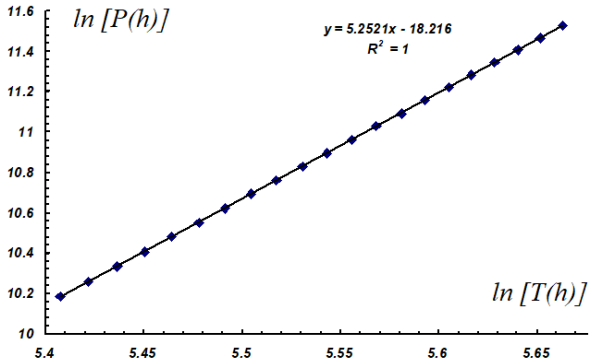


Fig.5 *The functional dependence* $\ln[P(h)] = f(\ln[T(h)]$

The correlation calculation of the linear dependence shows that

$$\frac{\gamma}{\gamma-1} = 5{,}2521 \Rightarrow \gamma = \frac{5{,}2521}{4{,}2521} \approx 1{,}23$$

The obtained result of the adiabatic constant of the atmospheric air is of the same order of the results of the papers [15],[16]. In order to check the barometric formula (5) for the troposphere air it would be better to represent this expression by the logarithm of this expression. The linear dependence will validate the expression of the barometric formula: $\ln[P(h)] = \ln[P_o] - \frac{M.g}{R.T}.h$. The graphic of $\ln[P(h)] = f(h)$ is represented on Fig. 6.

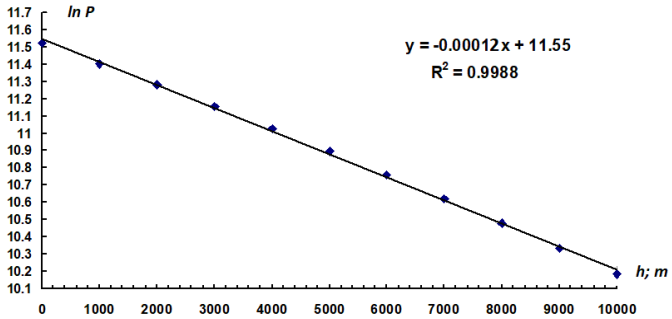


Fig. 6 *The graphic of the dependence* $\ln[P(h)] = f(h)$

The respective slope is: $\frac{M.g}{R.T} = 0{,}00012$. Then the calculation of the molar mass of troposphere air is: $M = \frac{0{,}00012\cdot 8{,}31\cdot 288}{9{,}83} = 0{,}02921(kg/mole)$

The calculated value of the molar mass of the troposphere air is of the same order like in [11].

$$\ln P_0 = 11{,}55 \Rightarrow \quad P_0 = 103777(Pa) \approx 1{,}04\cdot 10^5(Pa)$$

The obtained value of the pressure of the troposphere air at the null level is of the same order of the value from the Table 1 [11].

The graphic of $\ln[T(h)] = f(h/T)$ is represented on the Fig.7.

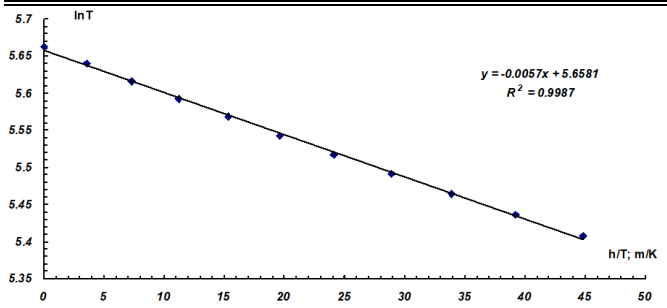


Fig. 7 *The graphic of the dependence* $\ln[T(h)] = f(h/T)$

The correlational calculations show that :

$$\ln[T(0)] = \frac{(\gamma-1)}{\gamma}\cdot(\ln P_o - \ln(const)) = 5{,}6581$$

$$\ln[T(0)] = 5{,}6581; \quad T(0) = e^{5{,}6581} = 286{,}6(K);$$

The respective slope of the graphic is: $-\frac{Mg\cdot(\gamma-1)}{R\cdot\gamma} = -0{,}0057$

Then, easily we can recalculate the molar mass of the troposphere air:

$$M = \frac{0{,}0057.R.\gamma}{g.(\gamma-1)} = \frac{0{,}0057\cdot 8{,}31\cdot 1{,}2}{9{,}83\cdot 0{,}2} = 0{,}0289(kg/mol)$$

The suggested method of the quantitative description of the variation of the atmospheric temperature ΔT with the increasing of the concentration of greenhouse gas CO_2 can be checked by the following Table 2 that is based on the results of the sources [13], [14].

Table 2. *The variation of temperature as the function of the increasing of the concentration of* CO_2

N°	year	ΔT; °C	C (CO_2); ppm	ΔC (CO_2); ppm	ΔC (CO_2); mg/m^3
0	1980	0	338	0	0
1	1981	0,03	340	2	3,61
2	1982	0,05	341	3	5,41
3	1983	0,07	343	5	9,01
4	1984	0,09	345	7	12,63
5	1985	0,11	347	9	16,23
6	1986	0,13	348	10	18,03
7	1987	0,15	349	11	19,84
8	1988	0,18	350	12	21,64
9	1989	0,19	350.5	12.5	22,54
10	1990	0,22	351	13	23,44
11	1991	0,26	352	14	25,25
12	1992	0,32	353	15	27,05
13	1993	0,34	355	17	30,66
14	1994	0,36	357	19	34,26
15	1995	0,37	359	21	37,87
16	1996	0,39	360	22	39,67
17	1997	0,41	361	23	41,48
18	1998	0,42	362	24	43,28
19	1999	0,43	363	25	45,08
20	2000	0,45	365	27	48,69
21	2001	0,46	369	31	55,90
22	2002	0,47	373	35	63,12
23	2003	0,5	375	37	66,72
24	2004	0,54	376	38	68,52
25	2005	0,58	378	40	72,13
26	2006	0,59	379	41	73,93
27	2007	0,6	380	42	75,74
28	2008	0,61	381	43	77,54
29	2009	0,62	382	44	79,34
30	2010	0,63	383	45	81,15
31	2011	0,65	385	47	84,75
32	2012	0,68	393	55	99,18
33	2013	0,7	398	60	108,20
34	2014	0,74	401	63	113,61
35	2015	0,78	402	64	115,41
36	2016	0,8	406	68	122,63
37	2017	0,81	410	72	129,84
38	2018	0,82	412	74	133,44
39	2019	0,83	413	75	135,25
40	2020	0,85	415	77	138,85

The usually concentrations that are represented on the Table 2 as *mmp* values can be transformed into *mg/m*^{3} by the application of the method given in [16]. So, the respective variation of *ppm* is:

$$\Delta C_{ppm} = \frac{24{,}4(l/mole)\cdot\Delta C[mg/m^3]}{M[g/mole]}$$

The variation of the concentrations of carbon dioxide ΔC[mg/m^3] in the atmosphere: $\Delta C[mg/m^3] = \frac{M[g/mole]\cdot\Delta C_{ppm}}{24{,}4}$

The respective dependence of the variation of the temperature ΔT as the function of ΔC is represented on the Fig. 8.

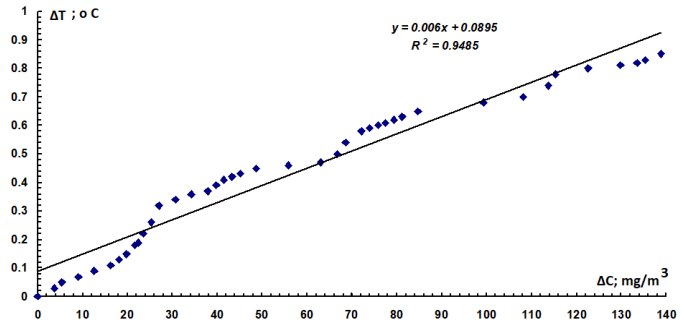


Fig. 8 *The graphic of the dependence* $\Delta T = f(\Delta C)$

The respective slope of the graphic ΔT=f(ΔC) is: $\left(\frac{\gamma-1}{\gamma(R-1)+1}\right)\cdot\frac{T}{C}=0{,}006$

The atmospheric air has the concentration:

$$C=0{,}04137(mol/l)=41{,}37(mol/m^3)\equiv 29(g/mol).41{,}37(mol/m^3)=$$
$$=1199{,}73(g/m^3)=1{,}199(kg/m^3)$$

The value of adiabatic constant γ is calculated from the expression below:

$$\left(\frac{\gamma-1}{\gamma(R-1)+1}\right)=\frac{0{,}006.C}{T}=\frac{0{,}006.1199{,}73}{288}=0{,}02499;$$

$$\gamma=\frac{1+0{,}02499}{1-0{,}02499\cdot(8{,}31-1)}=\frac{1{,}02499}{1-0{,}1826}=\frac{1{,}02499}{0{,}8174}=1{,}25$$

Such a way, the expression (16) could be written simply by proportional linear coefficient *a* as:

$\Delta T_e=a.\Delta C+0{,}0895$; (e)-empirical

$$a=\left(\frac{\gamma-1}{\gamma(R-1)+1}\right)\cdot\frac{T}{C}=\frac{1{,}25-1}{1{,}25.7{,}31+1}\cdot\frac{288}{1199{,}73}=$$
$$=\frac{0{,}25}{10{,}1375}\cdot\frac{288}{1199{,}73}=\frac{72}{12162{,}2628}=0{,}006$$
$$\Delta T_e=0{,}006\cdot\Delta C+0{,}0895;\quad [\Delta C]=mg/m^3;$$

The calculated values of ΔT_e can be checked with the real variations of ΔT by the representation of the following graphic. (Fig. 9)

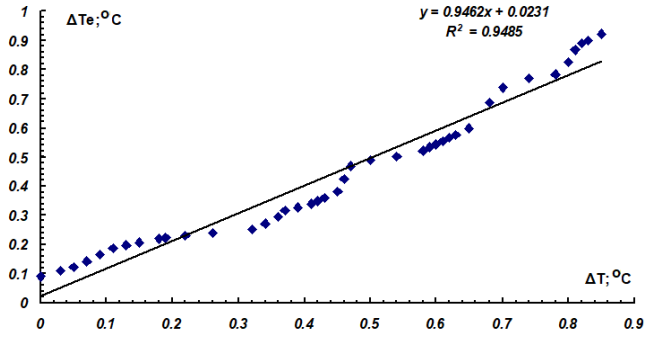


Fig. 9 *The validity of empirical calculations of temperature variations*

In order to have the important parameter like interval of time that can be included into the empirical expression, is necessary to represent the following dependence of the variation of concentration of carbon dioxide as the function of time (Fig. 10). The rate of increasing of CO_2 (speed of increasing of the concentration each year) is about *3,383((mg/m³)/year)*

Such a way the empirical formula of the temperature variation can be written as:

$$\begin{cases}\Delta T_e(t)=0{,}006\cdot\Delta C(t)+0{,}0895\\ \Delta C(t)=3{,}3833\cdot t-8{,}6206;\\ [t]=years;\quad [\Delta C]=mg/m^3\end{cases};$$

If each last years the concentration of carbon dioxide is increasing with the value of *3,383 mg/m³*, then it would give the possibility to calculate the excess mass Δm_{CO2} per year.

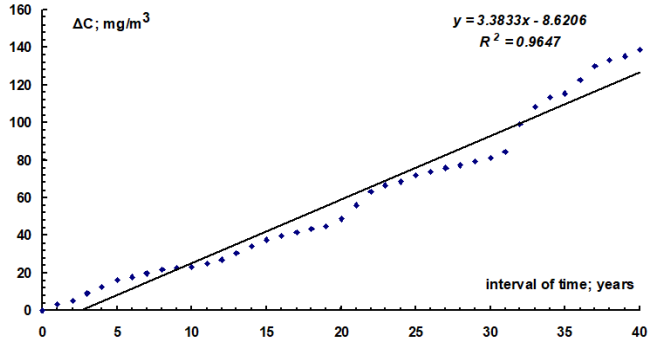


Fig. 10 *The variation of the concentration of carbon dioxide as the function of time (starting year is 1980)*

$$\Delta m_{CO_2}=\Delta C.V_{atm}=3{,}383((mg/m^3)/year).4{,}27596.10^{18}(m^3)=$$
$$=14{,}47.10^{18}(mg/year)=14{,}47.10^{12}(kg/year)=$$
$$14{,}47.10^{9}(tons/year)=14{,}47(Gtons/year)$$

The study [15] has such result about carbon dioxide: "Between 2009-18, however, the growth rate has been 2.3 ppm per year". Transposing *ppm* into mg/m³, then:

$$\Delta C[mg/m^3]=\frac{M[g/mole]\cdot\Delta C_{ppm}}{24{,}4}=\frac{44.2{,}3}{24{,}4}=4{,}14((mg/m^3)/year)$$

The result in this recent paper is 3,383 (mg/m³)/year. Then, the average value is 3,76 (mg/m³)/year. The respective admissible error is: $\varepsilon=\frac{|4{,}14-3{,}76|}{3{,}76}\cdot 100\%=\frac{38}{3{,}76}\approx 10\%$

This ready performed suggested empirical expression is only actually. It describes recently the global ecological state. The task is the reduction of the rate of emissions of CO_2 by the application of other types of energy resources.

Conclusions

The important task of the World's population nowadays is to maintain at least the same level of carbon dioxide concentration in the atmosphere and just to decrease it, because the consequences in the future are very unpleasant from healthy point of view both for the biosphere in general and for the human being in particular. Therefore, in order to know the current state of the atmosphere with the recent concentration of carbon dioxide, it is necessary to know the variation of the concentration over time. This study suggests a model based on thermodynamical theory of adiabatic processes in the atmosphere and the result is the achievement of an empirical expression of the temperature variation as a function of the concentration. The validation of the empirical expression is finalized with the calculation of the excess mass of carbon dioxide which is of the order of the real one like 15 billion tons per year.

The aim and the researched problem of the suggested method in this study are achieved. The values of molar mass and adiabatic constant are re-calculated and the method is generally validated. An important moment in this study is that as ΔC = 0, i.e. the concentration will not increase, then the temperature is set at a constant value at the given moment. It is clear that the method of the stopping of the accumulation of carbon dioxide can be achieved by the methods of the increasing of forest areas and the respective amount of carbon dioxide can be reduced by the process of photosynthesis. The classical method of using of fuels can be replaced by the application of non-traditional sources of energy such as the large application of the solar energy and of the new technologies that have more transformation efficient of this energy.

References

1. Haynes, H. M., ed. (2016–2017), CRC Handbook of Chemistry and Physics (97th ed.), CRC Press, p. 14, ISBN 978-1-4987-5428-6.

2. Jacobson, Mark Zachary (2005), Fundamentals of Atmospheric Modeling (2nd ed.) Cambridge University Press, ISBN 978-0-521-83970-9.

3. Ahrens, C. Donald (2006). Meteorology Today (8th ed.),Publishing. ISBN 978-0-495-01162-0.

4. Danielson, Levin and Abrams (2003). Meteorology. McGraw Hill.

5. Glossary of meteorology

https://glossary.ametsoc.org/wiki/Adiabatic_l pse_rate

6. Landau and Lifshitz (1980). Statistical Physics. Part 1. Pergamon.

7. Kittel and Kroemer (1980). Thermal Physics. Freeman. chapter 6, problem 11.

8. Lydolph, Paul E. (1985). The Climate of the Earth. Rowman and Littlefield Publishers Inc. p.12.

9. Landau and Lifshitz, Fluid Mechanics, Pergamon, 1979

10. Lide, David R. Handbook of Chemistry and Physics, Boca Raton, FL: CRC, 1996: 14–17

11. U.S. Standard Atmosphere (engineeringtoolbox.com), https://www.engineeringtoolbox.com/standard-atmosphere-d_604.html

12. Rebecca Lindsey and LuAnn Dahlman, "Climate Change: Global Temperature" , March 15, 2021, Climate Change: Global Temperature | NOAA Climate.gov

13. World of Change: Global Temperatures (nasa.gov)

14. "Last four years have been the warmest on record – and CO2 continues to rise", 7th January 2019, // Last four years have been the warmest on record – and CO2 continues to rise | Copernicus

15. Rebecca Lindsey, "Climate Change: Atmospheric Carbon Dioxide", (2020), https://www.climate.gov/news-features/understanding-climate/climate-change-atmospheric-carbon-dioxide

16. Air pollution workbook, Introduction to Air Pollution - Workbook (utoledo.edu)

Smoluchowski's coagulation equation with injections: applications to clustering of nano-particles

Dmitri V. Alexandrov[1,*], Ilya O. Starodumov[1], Sergei Fedotov[2],
Alexander A. Ivanov[1], Irina V. Alexandrova[1], Eugenya V. Makoveeva[1]
Ural Federal University, Ekaterinburg, Russian Federation[1]
The University of Manchester, Manchester, UK[2]
Dmitri.Alexandrov@urfu.ru

Abstract: *The coagulation equation, proposed by Smoluchowski, has been widely used to describe aggregation phenomena in many fields of science since its inception. It considers a physical system of many particles, and each particle is characterized by a change of some non-negative scalar quantity (e.g. volume). Assuming such a system to be spatially homogeneous and unbounded, considering only pairwise interactions and a balance relation of interacting particles, the Smoluchowski equation can be used to describe the evolution of a system of many particles. In this study, we construct an exact solution to this integro-differential equation containing an exponentially-decaying source term. This solution, in particular, describes the steady-state structural density of endosomes per cell carrying the nanoparticles (particles smaller than 100 nm). In addition, we derived an exact analytical solution to the unsteady-state coagulation equation in the Laplace transform image space. This solution can be inverted using numerical methods for Laplace transform inversion. For practical use, we derive an analytical solution to the non-stationary coagulation equation stitching the steady-state and initial distributions of structural density. Choosing the particular form of stitching functions, we demonstrate that the nonstationary solution evolves between the initial and steady-state distribution functions. Thus, analytical solutions obtained represent a general theoretical basis to describe the dynamics of cargo distributions in the endosomal network.*

Keywords*: COAGULATION, NANO-PARTICLES, CLUSTERING, ENDOSOMES*

1. Introduction

An important tool of modern medical technologies is nanoparticles (particles that do not exceed 100 nanometers in size). Such particles, for example, are intensively used in nanodiagnostics [1], radiation therapy for cancer treatment [2], as well as for targeted drug delivery to certain organs or cells of the body [3, 4]. In addition, nanoparticles are intensively used in gene therapy to develop effective treatments for many diseases [5].

The effectiveness of the use of nanoparticles is determined by the mechanisms of transfer of such particles in living cells, where their definite distribution is formed [6]. For example, the increase in the radiation dose largely depends on the intracellular distribution of gold nanoparticles (GNPs) [7, 8]. This suggests that the known distribution of GNPs within living cells can be used to control radiotherapy to treat diseases [9-13]. Note that GNPs are not uniformly distributed within cells and their distribution depends on the observation time [14-17]. It is also important that GNPs mainly accumulate in endosomes [18]. Initially, clusters of GNPs penetrate and accumulate inside the cell in the form of primary endocytic vesicles, which transport nanoparticles to early endosomes [18, 19]. Then, intracellular transport of early endosomes leads to aggregation of GNPs due to coagulation of endosomes. Note that the mechanism of cluster formation and evolution is caused by the mechanism of endosome fusion rather than the self-aggregation of GNPs.

In this article, we investigate the process of clustering nanoparticles inside endosomes based on the integro-differential coagulation equation with a source term. Previously, a similar mathematical model was used by Foret et al. [20]. The authors of this article deduced asymptotic distribution of endosome intracellular density based on the Smoluchowski integro-differential equation [21-24]. They showed that the asymptotic stationary density decreases with increasing cluster size in accordance with a power law with an exponential cut-off. In this study, we derive the exact analytical solution of the stationary coagulation equation, as well as construct an approximate solution of the nonstationary coagulation equation based on the stitching of known distributions.

2. The Model

An important circumstance is that nanoparticles enter early endosomes, and then they pass into late endosomes and lysosomes. The mathematical model developed below is based on the assumption that the clustering of nanoparticles occurs after the fusion of endosomes during their intracellular transport. To describe the mechanisms of coagulation and clustering of nanoparticles, we use the Smoluchowski integro-differential equation. Let each endosome contains y nanoparticles, where y is a continuous variable. Let us introduce the structural density of endosomes per cell $w(y,t)$, where t is time. Then the total number of endosomes $\mu(t)$ containing nanoparticles and nanoparticles inside a cell are determined by the integrals

$$\mu(t) = \int_0^\infty w(y,t)dy, \tag{1}$$

$$W(t) = \int_0^\infty yw(y,t)dy. \tag{2}$$

The structural density $w(y,t)$ is defined by the Smoluchowski integro-differential equation with a source term

$$\frac{\partial w}{\partial t} = \frac{1}{2}\int_0^y Z(y-y',y')w(y',t)w(y-y',t)dy' - w(y,t)\int_0^\infty Z(y,y')w(y',t)dy' + R(y) - \gamma(y)w(y,t). \tag{3}$$

Here $R(y)$ stands for the injection rate of new endosomes containing y nanoparticles, and $\gamma(y)$ is the rate of exocytosis of endosomes.

The initial structural density should be considered as known, i.e.

$$w(y,0) = w_0(y). \tag{4}$$

For the sake of simplicity, parameters Z and γ can be considered as constants [20], and a source term is given by [20]

$$R(y) = \frac{H}{y_0^2}\exp\left(-\frac{y}{y_0}\right), \qquad H = \int_0^\infty yR(y)dy. \tag{5}$$

Here H designates the total flux of endosomes.

Note that the aforementioned model has the asymptotic power-law stationary distribution [20]

$$w_{st} \sim y^{-\frac{3}{2}}, \qquad y \gg y_0. \tag{6}$$

Below we demonstrate how to find an exact steady-state solution valid for arbitrary values of variable y. To do this, we introduce the dimensionless variables as follows

$$\tau = Zt, \quad \kappa = \frac{\gamma}{Z}. \tag{7}$$

Here we assume that Z and γ are constant.

Now equation (3) can be rewritten in dimensionless form as

$$\frac{\partial w}{\partial \tau} = \frac{1}{2}\int_0^y w(y',\tau)w(y-y',\tau)dy' - \mu(\tau)w(y,t) + Q\exp\left(-\frac{y}{y_0}\right) - \kappa w(y,\tau), \quad Q = \frac{H}{y_0^2 Z}. \tag{8}$$

Equation (8) can be solved using the well-known Laplace transform

$$\widetilde{w}(p,\tau) = \int_0^\infty w(y,\tau)\exp(-py)dy. \tag{9}$$

Rewriting equation (8) in the Laplace space, we obtain

$$\frac{d\widetilde{w}}{d\tau} = \frac{\widetilde{w}^2}{2} - [\mu(\tau)+\kappa]\widetilde{w} + \frac{Qy_0}{1+y_0 p}. \tag{10}$$

The total number of endosomes $\mu(\tau)$ can be found from equation (10) at $p = 0$

$$\frac{d\mu}{d\tau} = -\frac{\mu^2(\tau)}{2} - \kappa\mu(\tau) + Qy_0. \tag{11}$$

3. Analytical Solutions

In this section, we consider the steady-state and unsteady-state cases of the structural density of endosomes per cell.

Steady-state scenario.

The stationary value of total number of endosomes μ_{st} can be determined from equation (11) and takes the form

$$\mu_{st} = \sqrt{2Qy_0 + \kappa^2} - \kappa. \tag{12}$$

Now taking $d\widetilde{w}/d\tau = 0$ into account, we get the structural density in the Laplace space from equation (10) with allowance for the steady-state solution (12)

$$\widetilde{w}_{st} = \alpha - \sqrt{\alpha^2 - \frac{2Qy_0}{1+y_0 p}}, \quad \alpha = \sqrt{2Qy_0 + \kappa^2}. \tag{13}$$

Multiplying and dividing the r.h.s. of equation (13) by the conjugate expression

$$\alpha + \sqrt{\alpha^2 - \frac{2Qy_0}{1+y_0 p}},$$

we rewrite (13) in the form of

$$\widetilde{w}_{st} = \frac{2Q}{\alpha\left[p+\beta' + \sqrt{(p+\beta')(p+\alpha')}\right]}, \tag{14}$$

$$\alpha' = \frac{1}{y_0} - \frac{2Q}{\alpha^2}, \quad \beta' = \frac{1}{y_0}.$$

Inverting expression (14), we arrive at the steady-state structural density [25]

$$w_{st}(y) = \frac{Q}{\alpha}\exp\left(-\frac{\alpha'+\beta'}{2}y\right)\left[I_1\left(\frac{\alpha'-\beta'}{2}y\right) + I_0\left(\frac{\alpha'-\beta'}{2}y\right)\right]. \tag{15}$$

Here I_0 and I_1 represent the modified Bessel functions.

An important point is that the asymptotic behaviour of the structural density (15) at large y coincides with the power-law expression found by Foret et al. [20], i.e. $w_{st} \sim y^{-3/2}$. To derive this asymptotic behaviour, we use the following formulas

$$I_0(-\lambda) = I_0(\lambda), \quad I_1(-\lambda) = -I_1(\lambda), \tag{16}$$

$$I_0(\lambda) \simeq \frac{\exp(\lambda)}{\sqrt{2\pi\lambda}}\left(1+\frac{1}{8\lambda}\right), \quad I_1(\lambda) \simeq \frac{\exp(\lambda)}{\sqrt{2\pi\lambda}}\left(1-\frac{3}{8\lambda}\right) \tag{17}$$

at large λ.

Now combining (15)-(17), we get

$$w_{st}(y) \simeq \frac{Q}{2\alpha}\frac{\exp(-my)}{\sqrt{2\pi}}\left(\frac{Q}{\alpha^2}\right)^{-3/2} y^{-3/2}, \tag{18}$$

where

$$m = \frac{\kappa^2}{y_0(2Qy_0+\kappa^2)}.$$

The steady-state and asymptotic structural densities (15) and (18) are compared in Fig. 1. As is easily seen, the previously known asymptotic distribution (18) [20] differs significantly from the exact analytical solution (15). As this takes place, the most significant difference occurs when the number of nanoparticles y is small enough.

Unsteady-state scenario.

Introducing the new function $\tilde{y}(p,\tau) = \widetilde{w}(p,\tau) - \mu(\tau) - \kappa$ and taking the initial condition $\widetilde{w}(0) = \widetilde{w}_0$ into account, we arrive at the following Riccati equation

$$\frac{d\tilde{y}}{d\tau} = \frac{\tilde{y}^2}{2} + \frac{Qy_0}{1+y_0 p} - \frac{[\mu(\tau)+\kappa]^2}{2} - \frac{d\mu}{d\tau} \tag{19}$$

supplemented with the initial condition $\tilde{y}(0) = \widetilde{w}_0 - \mu(0) - \kappa$.

Now integrating equation (11), we obtain $\mu(\tau)$ in the case of unsteady-state growth scenario

$$\mu(\tau) = \frac{\alpha - \kappa + (\alpha+\kappa)h(\tau)}{1-h(\tau)}, \tag{20}$$

where

$$h(\tau) = \frac{\mu(0)+\kappa-\alpha}{\mu(0)+\kappa+\alpha}\exp(-\alpha\tau), \mu(0) = \int_0^\infty w_0(y)dy.$$

Setting $\kappa = 0$ and $\mu(0) = 0$, we come to the following analytical expression

$$\mu(\tau) = \sqrt{2Qy_0}\tanh\left(\sqrt{\frac{Qy_0}{2}}\tau\right), \tag{21}$$

where $\sqrt{2Qy_0} = \mu_{st}$ at $\kappa = 0$.

Combining (11) and (19), we arrive at the following equation for the shifted structural density

$$\frac{d\tilde{y}}{d\tau} = \frac{\tilde{y}^2 - \kappa^2}{2} - \frac{Qy_0^2 p}{1+y_0 p}. \tag{22}$$

An exact analytical solution of this equation can be expressed in the form of

$$\tilde{y}(p,\tau) = s\frac{(\tilde{y}(0)+s)\exp(-s\tau) + \tilde{y}(0) - s}{(\tilde{y}(0)+s)\exp(-s\tau) - (\tilde{y}(0)-s)}, \tag{23}$$

where

$$s = \sqrt{\kappa^2 + \frac{2Qy_0^2 p}{1+y_0 p}}.$$

If $\kappa = 0$ and $\tilde{y}(0) = 0$, expression (23) reads as

$$\widetilde{w}(p,\tau) = \mu(\tau) - s_0\tanh\left(\frac{s_0}{2}\tau\right), \tag{24}$$

where

$$s_0 = \sqrt{\frac{2Qy_0^2 p}{1+y_0 p}}.$$

Let us especially emphasize that the inverse Laplace transforms of equations (23) and (24) are unknown. These equations can be inverted numerically [26]. However, such a problem represents a separate research problem.

Keeping this in mind, we consider another method for constructing the analytical solution for a nonstationary structural density $w(y,t)$. Note that $w(y,t)$ lies between the known initial distribution function $w_0(y)$ and the stationary structural density (15), to which $w(y,t)$ approaches with increasing time. Taking this behaviour into account, we apply the stitching method for analytical dependences $w_0(y)$ and $w_{st}(y)$ [27, 28]. According to this method, the structural density can be written as a function of the following form [28, 29]

$$w(y,\tau) = \frac{b_0(\tau)w_0(y)}{b_0(\tau)+b_{st}(\tau)} + \frac{b_{st}(\tau)w_{st}(y)}{b_0(\tau)+b_{st}(\tau)} = \frac{w_0(y)}{1+\frac{b_{st}(\tau)}{b_0(\tau)}} + \frac{w_{st}(y)}{1+\frac{b_0(\tau)}{b_{st}(\tau)}}, \quad (25)$$

where $b_0(\tau)$ and $b_{st}(\tau)$ represent the stitching functions. These functions should behave as follows: $b_0(\tau) \to 0$ at $\tau \gg 1$, and $b_{st}(\tau) \to 0$ at $\tau \to 0$. An important point is that $b_0(\tau)$ and $b_{st}(\tau)$ should be selected from the condition that the theory is consistent with experimental data.

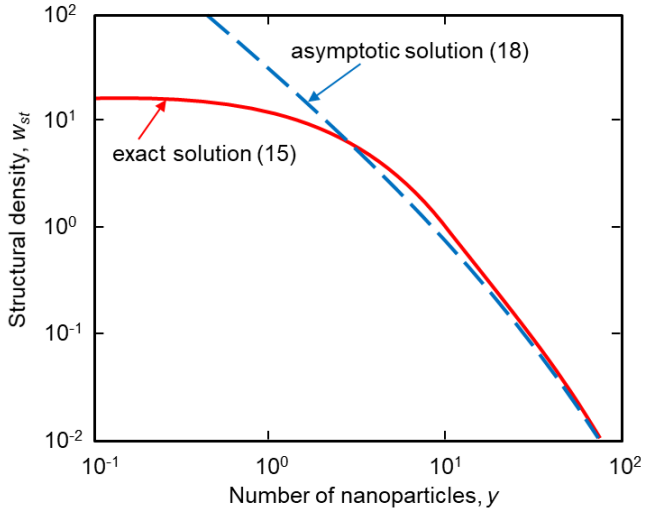


Fig. 1 *The steady-state structural density w_{st} (solid line) and its asymptotic value (dashed line) plotted accordingly to expressions (15) and (18), respectively. Physical parameters are: $Z = 10^{-4}$ s^{-1}, $\gamma = 0.0015$ s^{-1}, $x_0 = 2$, $H = 0.5$ s^{-1}.*

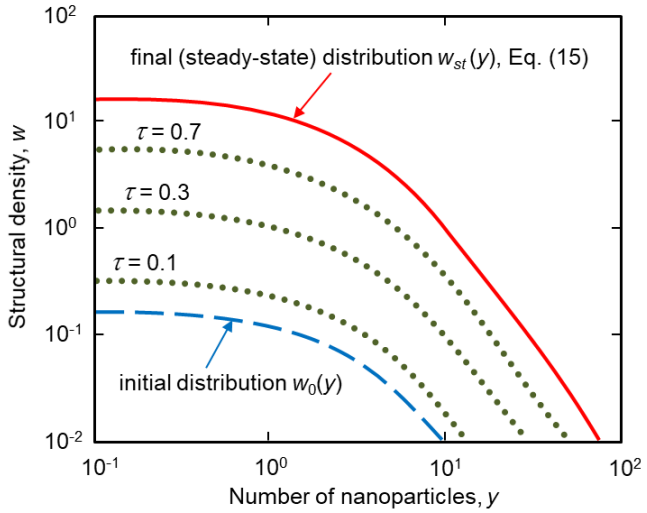


Fig. 2 *The relaxation dynamics of $w(y,\tau)$ between the initial $w_0(y) = \varepsilon w_{st}(y)$ and steady-state $w_{st}(y)$ distributions ($\varepsilon = 0.01$). Physical parameters correspond to Fig. 1.*

In Fig. 2, we illustrate the evolutionary behaviour of our unsteady-state analytical solution (25) for $b_0(\tau) = 1/\tau$ and $b_{st}(\tau) = \tau$. In this case, expression (25) takes the form

$$w(y,\tau) = \frac{w_0(y)}{1+\tau^2} + \frac{\tau^2 w_{st}(y)}{1+\tau^2}. \quad (26)$$

It is significant that the structural density $w(y,\tau)$ at small times coincides with the initial distribution function $w_0(y)$. At large times, the structural density $w(y,\tau)$ asymptotically tends to its stationary solution $w_{st}(y)$. In all other cases (at $0 < \tau < \infty$), this function is between the initial and stationary distributions. For a more accurate description of nanoparticle dynamics in cells, it is necessary to compare the analytical theory under consideration with experiments on nanoparticle transport in living cells (e.g., with [29]). Such a comparison is the subject of future research.

4. Conclusion

In summary, we consider the theory of nanoparticle clustering in living cells using the integro-differential coagulation equation with a source term. In this paper, we have constructed an exact analytical solution of the steady-state model when the source term is exponentially damped. In the case of unsteady-state clustering, the model equations are solved in the Laplace transform image space. For practical purposes, the analytical solution of the nonstationary model is constructed using the initial and stationary structural densities stitching. This stitched solution evolves between the initial and final (steady-state) distributions.

5. Acknowledgements

DVA, IOS, AAI, IVA and EVA are grateful to the Ministry of Science and Higher Education of the Russian Federation for the financial support (project no. 075-15-2021-1002). SF acknowledges financial support from EPSRC Grant No. EP/V008641/1.

6. References

1. S.-m. Park, A. Aalipour, O. Vermesh, J.H. Yu, S.S. Gambhir, Nature Reviews Materials 2, 1 (2017)
2. J.F. Hainfeld, D.N. Slatkin, H.M. Smilowitz, Phys. Med. Biol. 49, N309 (2004)
3. P. Ghosh, G. Han, M. De, C.K. Kim, V.M. Rotello, Advanced Drug Delivery Reviews 60, 1307 (2008)
4. M.J. Mitchell, M.M. Billingsley, R.M. Haley, M.E. Wechsler, N.A. Peppas, R. Langer, Nature Reviews Drug Discovery 20, 101 (2021)
5. K.A. Whitehead, R. Langer, D.G. Anderson, Nat. Rev. Drug Discovery 8, 129 (2009)
6. F.-Y. Kong, J.W. Zhang, R.-F. Li, Z.-X. Wang, W.-J. Wang, W. Wang, Molecules 22, 1445 (2017)
7. Y. Lin, S.J. McMahon, H. Paganetti, J. Schuemann, L. Yuting, J.M. Stephen, P. Harald, S. Jan, Phys. Med. Biol. 60, 4149 (2015)
8. W. Sung, S.-J. Ye, A.L. McNamara, S.J. McMahon, J. Hainfeld, J. Shin, H.M. Smilowitz, H. Paganetti, J. Schuemann, Nanoscale 9, 5843 (2017)
9. K. Haume, S. Rosa, S. Grellet, M.A. Smiałek, K.T. Butterworth, A.V. Solov'yov, K.M. Prise, J. Golding, N.J. Mason, Cancer Nanotechnol. 7, 8 (2016)
10. S. Her, D.A. Jaffray, C. Allen, Adv. Drug Deliv. Rev. 109, 84 (2017)
11. D. Peukert, I. Kempson, M. Douglass, E. Bezak, Phys. Med. 47, 121 (2018)
12. B. Villagomez-Bernabe, F.J. Currell, Sci. Rep. 9, 1 (2019)
13. B. Villagomez-Bernabe, J. Ramos-Méndez, F.J. Currell, Cancers 13, 2034 (2021)
14. D.B. Peckys, N. de Jonge, Nano Lett. 11, 1733 (2011)
15. D.B. Peckys, N. de Jonge, Microsc. Microanal. 20, 189 (2014)
16. E. Sadauskas, N.R. Jacobsen, G. Danscher, M. Stoltenberg, U. Vogel, A. Larsen, W. Kreyling, H. Wallin, Chem. Cent. J. 3, 16 (2009)

17. L. Stefančíková, E. Porcel, P. Eustache, S. Li, D. Salado, S. Marco, J.L. Guerquin-Kern, M. Réfrégiers, O. Tillement, F. Lux, S. Lacombe, Cancer Nanotechnol. 5, 6 (2014)
18. M. Liu, Q. Li, L. Liang, J. Li,k. Wang, J. Li, M. Lv, N. Chen, H. Song, J. Lee, J. Shi, L. Wang, R. Lal, C. Fan, Nat. Commun. 8, 15646 (2017)
19. S.H. Wang, C.W. Lee, F.G. Tseng, K.K. Liang, P.K. Wei, J. Biophotonics 9, 738 (2016)
20. L. Foret, J.E. Dawson, R. Villaseñor, C. Collinet, A. Deutsch, L. Brusch, M. Zerial, Y. Kalaidzidis, F. Jülicher, Current Biology 22, 1381 (2012)
21. S. Cueille, C. Sire, Phys. Rev. E. 57, 881 (1998)
22. H. Hayakawa, J. Phys. A: Math. Gen. 20, L801 (1987)
23. H. Takayasu, Phys. Rev. Lett. 63, 2563 (1989)
24. D.V. Alexandrov, Int. J. Heat Mass Trans. 121, 884 (2018)
25. V.A. Ditkin, A.P. Prudnikov, *Integral transforms and operational calculus* (Pergamon Press, 1965)
26. A.M. Cohen, *Numerical methods for Laplace transform inversion* (Springer, 2007)
27. A.H. Nayfeh, *Perturbation methods* (Wiley-VCH, 2000)
28. D.V. Alexandrov, P.K. Galenko, Phil. Trans. R. Soc. A, 378, 20190243 (2020)
29. S.H. Wang, C.W. Lee, F.G. Tseng, K.K. Liang, P.K. Wei, J. Biophotonics 9, 738 (2016)